

Final Draft
of the original manuscript:

Bolz, S.; Oehring, M.; Lindemann, J.; Pyczak, F.; Paul, J.; Stark, A.;
Lippmann, T.; Schrufer, S.; Roth-Fagaraseanu, D.; Schreyer, A.; Weiss, S.:

**Microstructure and mechanical properties of a forged
Beta-solidifying Gamma TiAl alloy in different heat treatment
conditions**

In: Intermetallics (2014) Elsevier

DOI: 10.1016/j.intermet.2014.11.008

Microstructure and mechanical properties of a forged β -solidifying γ TiAl alloy in different heat treatment conditions

S. Bolz^a, M. Oehring^b, J. Lindemann^c, F. Pyczak^{a,b}, J. Paul^b, A. Stark^b, T. Lippmann^b, S. Schrüfer^d, D. Roth-Fagaraseanu^d, A. Schreyer^b, S. Weiß^a

^aChair of Physical Metallurgy and Materials Technology, Brandenburg University of Technology Cottbus, Konrad-Wachsmann-Allee 17, D-03046 Cottbus, Germany

^bHelmholtz-Zentrum Geesthacht, Institute of Materials Research, Max-Planck-Str. 1, D-21502 Geesthacht, Germany

^cGfE Fremat GmbH, Lessingstr. 41, D-09599 Freiberg, Germany

^dRolls-Royce Deutschland Ltd & Co KG, Eschenweg 11, D-15827 Blankenfelde-Mahlow, Germany

Corresponding author: Dr. Michael Oehring, e-mail: michael.oehring@hzg.de,

Phone: +49 4152 87 2672, FAX: +49 4152 87 2534

e-mail-addresses:

sebastian.bolz@tu-cottbus.de

janny.lindemann@gfe.com

florian.pyczak@hzg.de

jonathan.paul@hzg.de

andreas.stark@hzg.de

thomas.lippmann@hzg.de

Susanne.Schruefer@Rolls-Royce.com

Dan.Roth-Fagaraseanu@Rolls-Royce.com

andreas.schreyer@hzg.de

sabine.weiss@tu-cottbus.de

Abstract

In the cast condition γ titanium aluminide alloys that solidify completely through the β phase are characterized by fine and homogeneous microstructures, weak textures and low segregation. For these reasons such alloys have a relatively good workability and can be closed-die forged without preceding ingot breakdown even if the alloys contain no large fractions of the β phase at the working temperature. The present work was devoted to a combined study of the constitution and microstructural morphologies that develop in various two-step heat treatments of a single-step forged β solidifying alloy. The study included high-energy X-ray diffraction for in situ investigations of the constitution at the heat treatment temperature. It was observed that the phase transformations are quite sluggish in the material which results in fine microstructures and some conditions that significantly deviate from thermodynamic equilibrium. Further, tensile and creep testing was carried out on the different material conditions in order to identify the range in which the properties can be varied. It is found that this easily forgeable material exhibits comparable strength, ductility and creep strength as more conventional peritectically solidifying alloys.

Keywords: A. titanium aluminides, based on TiAl. B. creep. B. mechanical properties at ambient temperature. B. phase transformation. C. themomechanical treatment. D. microstructure.

1 Introduction

Alloys based on the intermetallic phase γ -TiAl are increasingly being used as a light-weight high-temperature material [1, 2]. Despite more than two decades of research on these materials further progress is desired with respect to the damage tolerance, cost, processing reliability and creep resistance [3 - 6]. In recent years so-called β -solidifying alloys have emerged which completely solidify via the β phase and offer a couple of advantages [6 - 14]. In the cast condition such alloys exhibit fine and homogeneous microstructures, weak textures and little segregation [6, 8, 9, 10, 13]. This makes them attractive for cast applications, however, these features are also very beneficial with respect to wrought processing routes [6, 11]. If the alloys contain significant fractions of the β phase at the hot-working temperature, the workability is tremendously increased compared to conventional γ alloys [15, 16]. Tetsui,

Takeyama and co-workers have presented corresponding alloys that could be conventionally forged in cold dies, something which is not possible with usual TiAl alloys [15, 16]. Even if β solidifying alloys do not contain large fractions of the β phase at hot-working temperature, the materials have sufficiently fine microstructures so that they can be forged in closed dies without any preceding ingot breakdown [11, 17]. This is a sign of substantial progress in terms of material yield, cost and maximum component size that can be manufactured compared to wrought processing routes comprising both ingot break-down and secondary processing. However, β solidifying alloys are quite complex materials containing Ti, Al and β stabilizing elements like Nb, Mo etc. as well as B for grain refinement. This complexity certainly influences the constitution and new phases can arise as e.g. variants of the ω phase [18] or an orthorhombic phase with B19 structure [19]. Moreover, due to slowly diffusing alloying elements as Nb and Mo and the partitioning of these elements the phase transformation kinetics might be altered significantly compared to conventional γ alloys and unexpected microstructures could evolve. For this reason the present work was directed to a combined study of the constitution and microstructural morphologies resulting from various two-step heat treatments performed on a forged β solidifying alloy. In order to assess the resulting microstructures with respect to mechanical properties the heat-treatments were systematically varied and tensile and creep tests were carried out on all material conditions. The essential aim of the present study was to critically evaluate the capability of a forged β solidifying alloy with respect to use as a high-temperature material and to identify the range of microstructural variability and resultant mechanical properties.

2 Materials and experiments

Cast ingots of the alloy Ti-44.5Al-6.25Nb-0.8Mo-0.1B (in at.%) with a diameter of 50 mm and a length of around 200 mm were supplied by GfE in Nuremberg, Germany. The cast material had been produced by remelting a VAR ingot using a VAR skull melter and centrifugal casting into permanent moulds followed by hot-isostatic pressing (HIP) at 1210 °C and 200 MPa for 4 h. An energy-dispersive X-ray spectroscopy (EDX) analysis system (INCA, Oxford Instruments) that was attached to a ZEISS DSM962 scanning electron microscope (SEM) was employed to check the composition of the alloy. The EDX system was calibrated with an alloy standard of similar composition to the material under investigation. By analysing a systematic alloy series it was found that the concentration of the alloying elements could be measured with an accuracy of 0.15 at.%. With this system 4 EDX

analyses of an area of 4 mm² were carried out at different positions of one specimen which resulted in a mean composition of 44.5 at.% Al, 6.5 at.% Nb and 0.9 at.% Mo disregarding the B content. This indicates that the alloy is near the nominal composition, but an analysis of the average composition and the chemical homogeneity of the entire ingot has not been carried out. Oxygen and nitrogen analyses were carried out using the melt extraction technique (LECO analysis system) which yielded levels of 590 µg/g O and 80 µg/g N.

Cylindrical blanks of the cast material were isothermally forged to plates perpendicularly to the cylinder axis by Leistritz Turbinentechnik GmbH, Remscheid, Germany. The forging dies made of a Mo alloy were heated to 1200 °C, whereas the work pieces had been heated to 1270 °C immediately prior to forging. Forging was carried out under a nitrogen atmosphere to a height reduction of -0.64 to -0.7 for the central axis (corresponding to a logarithmic strain $\phi = -1.0$ to -1.2) using a strain rate of $5 \cdot 10^{-3} \text{ s}^{-1}$. Unless otherwise specified, after forging the plates were subjected to an annealing treatment of 6 h at 800 °C followed by furnace cooling in order to reduce internal stresses. Other forgings were produced from VAR ingot material that had been extruded in the ($\alpha + \gamma + \beta$) phase field and subsequently forged perpendicular to the extrusion direction. The extruded material was forged using the same conditions as the cast material. This extruded and forged material was only used for in situ high-energy X-ray diffraction (HEXRD) investigations.

Cylindrical test piece blanks with a diameter of 10 mm were cut from the forged and annealed plates using spark erosion. The blanks were orientated parallel to the axis of the former cast cylinders. All subsequent heat treatments were carried out on these blanks in order to ensure comparable cooling conditions. The heat treatments were conducted under air in a muffle furnace, the temperature of which was controlled by a type S thermocouple positioned close to the specimen. From the heat-treated blanks both tensile and creep specimens as well as specimens for microstructural analysis were machined. Since the gauge diameter of all specimen types was ≤ 5.3 mm, i.e. substantially smaller than the diameter of the blanks, any surface environmental influence of the heat treatments on the mechanical properties can be excluded.

The microstructure in the different processed conditions was characterized by scanning electron microscopy (SEM) using back-scattered electrons. For SEM a Tescan Mira II XMH microscope and the above mentioned Zeiss microscope were used. SEM specimens from heat-

treated material were cut perpendicularly to the long axis of the heat-treated blanks. Microstructural samples were taken with an image plane perpendicular to the long axis of the cast piece and parallel to the deformation axis of forged specimens, respectively. After cutting the specimens were ground and electro-polished at -19 V and -45 °C in a solution of 600 ml methanol, 300 ml n-butanol and 60 ml perchloric acid. Some of the microstructural specimens were polished in a vibrating polisher using colloidal silica as polishing agent.

Transmission electron microscopy (TEM) was employed to analyse structural changes as well as dislocation processes that took place during creep deformation. Specimens of 0.5 mm thickness were cut perpendicularly to the loading axis from the gauge length of crept specimens, ground to 0.15 mm thickness from both sides and electro-polished down to electron transparency with a twin-jet polisher (Fischione) at -19 V and -35 °C in a solution of 430 ml methanol, 250 ml n-butanol and 18 ml perchloric acid. For TEM a Philips CM200 microscope was used operating at 200 kV.

Prior to the heat treatments the alloy constitution was investigated in dependence of temperature by differential scanning calorimetry (DSC) and in situ heating high-energy X-ray diffraction (HEXRD) experiments. DSC runs were performed with a heating rate of 20 K/min under pure Ar (99.9999 %) using a Netzsch Pegasus 404C heat flux calorimeter. HEXRD was carried out using synchrotron radiation at the HARWI II beamline run by the Helmholtz-Zentrum Geesthacht at the Deutsches Elektronen-Synchrotron (DESY) in Hamburg [20]. Cylindrical specimens of extruded and forged material (\varnothing 4 mm) were inductively heated with a rate of 20 K/min under an Ar atmosphere in an in situ specimen environment consisting of a modified DIL 805/A type dilatometer from the company Bähr Thermoanalyse, Hüllhorst, Germany (now TA instruments, New Castle, DE, USA). The specimen temperature was controlled by a thermocouple directly spot-welded onto the specimen. During heating the specimen was transmitted by a synchrotron radiation beam with a cross-section of $1 \times 1 \text{ mm}^2$ and a photon energy of 100 keV, corresponding to a wavelength of 0.012398 nm. The diffracted radiation was detected by a mar555 flat panel detector. Diffractograms were obtained by azimuthal integration of the recorded Debye-Scherrer rings. Phase fractions were determined by Rietveld analysis of the XRD patterns using the MAUD software package [21]. HEXRD was also employed to analyse the structure of heat-treated specimens at room temperature. In this case, the same experimental set-up was used, except

that the specimens of some mm thickness were mounted on a specimen holder instead being inserted into the dilatometer

After undergoing heat treatments the blanks were machined into tensile specimens with a length of 55 mm and creep tensile specimens of 75 mm in length. Tensile testing was performed in a universal testing machine of Type Inspekt 100. Prior to tensile testing the specimens were electropolished at -19V and -25°C in a solution of 250 ml methanol, 180 ml 1-butanol and 30 ml perchloric acid. During tensile testing the strain was measured by a MFHT extensometer attached to the gauge length. The creep tests were carried out under air using constant lever arm creep testing frames (SATEC). The strain development during creep testing was measured by extensometry attached to the ridged specimens.

3 Results and discussion

3.1 Microstructure in the as-cast and forged condition

In the as-cast and HIPed condition the material showed a uniform microstructure consisting of relatively small lamellar colonies with a size of 30 to 100 μm , γ and β/β_0 grains and a small amount of Borides with a curvy morphology (Fig. 1a, b). Here β_0 designates the ordered variant of the β phase (A2 structure) with B2 structure. According to the chemical composition of the phases determined by EDX, the γ phase appears dark in the SEM images, the α_2 phase exhibits an intermediate brightness and the β/β_0 phase and Borides are the brightest phases. The fine and homogeneous cast microstructures as observed in Fig. 1a are typical for B containing γ alloys that solidify solely via the β phase [6, 7, 10, 11, 13]. After forging under the conditions described earlier the microstructure was refined and contains mainly equiaxed γ and β/β_0 grains and a few newly formed lamellar colonies. It should be noted that the HEXRD results presented later show that the forging temperature is within the ($\alpha + \gamma + \beta$) phase field. Some colonies with not fully recrystallized bent lamellae were observed (Fig. 1 c). Bending and kinking of lamellae has quite often been observed in γ alloys during hot working and induces strain localization which impedes recrystallization between the shear bands where relatively low strain energy is imparted [22 - 24]. This can result in pronounced microstructural inhomogeneities consisting of large lamellar regions which have not been recrystallized [24]. Alloys which have a starting microstructure of coarse lamellar colonies are especially susceptible to this effect, while alloys with an initial duplex or equiaxed microstructure exhibit faster recrystallization and fewer inhomogeneities after

working [24]. In comparison to many literature investigations [22 - 25], the observed microstructure after forging is quite homogeneous and a major fraction of the microstructure has been converted by recrystallization into equiaxed or newly formed lamellar constituents.

3.2 In situ heating investigation and phase constitution

In order to understand the microstructure development during heat treatment it is essential to know the dependence of phase constitution on temperature. In a first step, extruded and forged material was heated in the DSC with 20 K/min. The obtained DSC trace (Fig. 2) showed peaks at around 1200 °C, 1280 °C and 1420 °C, which were attributed after consulting the ternary Ti-Al-Nb phase diagram [26] to the eutectoid, γ solvus (α transus) and β transus temperatures, respectively. Identical material was heated in the synchrotron beam with the same heating rate and diffraction patterns were recorded every 10 K in order to unambiguously identify the phases occurring. The diffraction rings were integrated azimuthally and phase fractions were calculated from peak intensities. Due to the very weak texture and fine microstructure the material is well suited for phase fraction determination using Rietveld analysis of the diffractograms. The results are shown in Fig. 2 and include peaks associated with superlattice reflections of the ordered α_2 and β_0 phase, too. From these superlattice peaks it is clearly visible that at 1200 °C the α_2 phase is first to disorder followed by disordering of the β_0 phase at 1210 °C, i.e. the phase sequence $\alpha_2 + \beta_0 + \gamma \rightarrow \alpha + \beta_0 + \gamma \rightarrow \alpha + \beta + \gamma$ is observed over a small temperature interval. The in situ experiment further confirms the transition to the α phase at around 1300 °C, although a small fraction of the β phase can still be found at this temperature, and the transition to β beginning at 1380 °C. It should be noted that Fig. 2 exhibits a maximum of the β/β_0 phase fraction at about 1180 °C. In conclusion, the phase constitution appears to be elucidated by in situ HEXRD, however, there are minor phases with too low a volume fraction to be detected, as for example the Borides, which are certainly present in the material. Furthermore, the phase transformations might also be too sluggish for the applied heating rate and thus, the in situ experiment might not show the phase equilibrium of the material at the respective temperature. To gather additional information the constitution of different heat-treated specimens was inspected. Since the aim of the present work is obtaining lamellar colonies as the major microstructural constituent, a heat treatment temperature of 1270 °C slightly below the γ solvus temperature was selected. Specimens of extruded and forged material were heat-treated for 1 h at this temperature and then quenched into oil. Two of the specimens were subjected to a subsequent annealing

treatment of 6 h/800 °C or 2 h/ 1000 °C followed by furnace cooling. All specimens were then investigated by transmission HEXRD. The phase fractions determined by Rietveld analysis from the diffractograms are shown in Table 1. As obvious from table 1 the quenched sample predominantly consisted of the α_2 phase with a minor fraction of the γ phase and 2 vol.% β/β_0 . During annealing at 800 °C the fraction of the γ phase grew at the expense of the α_2 phase and at 1000 °C the fraction of the β/β_0 phase increased, too. The investigations generally confirm the constitution as described above and indicate that the phase composition significantly changes during the annealing treatments.

3.3 Microstructure in the different heat treatment conditions

From the foregoing investigations it was decided to examine 3 high-temperature (near α transus) heat treatment temperatures: (i) 1300 °C, in order to obtain fully or almost fully lamellar material, (ii) 1270 °C for nearly lamellar microstructures and (iii) 1250 °C for duplex microstructures. Since fast cooling can result in constitutions strongly deviating from the equilibrium as shown above, the influence of the cooling rate after the high-temperature heat treatment and two subsequent ageing treatments, 6 h/800 °C and 2 h/1000 °C, on the microstructure was investigated.

Fig. 3 shows the microstructure of forged specimens that were subjected to a heat treatment at 1250 °C, 1270 °C or 1300 °C, all followed by air cooling and an annealing treatment of 6 h/800 °C/furnace cooling. In the specimen heat-treated at the highest temperature a fully lamellar microstructure is observed, which has the largest colony size among the investigated specimens. At some colony boundaries of this sample bright β grains are found. Under closer examination it is evident, that small γ precipitates are incorporated in these β grains. These β grains prevent excessive growth of α grains but their density is too low to preserve the fine grain size of the as forged material. The two specimens heat-treated at lower temperatures exhibit a microstructure consisting of significantly smaller lamellar colonies, γ grains and partly seams of the γ phase at colony boundaries, as well as β/β_0 grains, which are subdivided by γ precipitates. With decreasing high-temperature heat treatment temperature the volume fraction of γ and β grains increased (Table 2 and 3). It has to be noted that the β phase cannot be distinguished from its ordered variant β_0 with B2 structure in the SEM images. In summary, by varying the high-temperature heat treatment temperature not only the size of lamellar colonies and the fraction of γ grains but also the morphology of the γ phase and the inner microstructure of β/β_0 phase regions are modified.

In order to study the influence of the cooling rate, forged specimens were heat treated at 1270 °C for 1 h, oil-quenched (OQ), air-cooled (AC) or furnace-cooled (FC) and then annealed (6 h/800 °C/FC). The microstructures obtained by these treatments are shown in Fig. 4. Apparently, the cooling rate has a strong influence on the microstructural morphology in this material. The oil-quenched specimen exhibited lamellar colonies, γ grains and β/β_0 grains, the latter showing many fine precipitates. For the air-cooled specimen lamellar colonies, γ grains and seams of the γ phase at colony boundaries were observed together with β/β_0 grains that contained only a few γ precipitates. The furnace-cooled material had only a relatively small fraction of lamellar colonies, a surprisingly high amount (61 %, see Table 2) of γ grains and some β/β_0 grains without γ precipitates. High or medium cooling rates obviously favour the precipitation of γ lamellae from the α phase, while at low cooling rates γ grains grow from the α phase grain boundaries. This behaviour can be understood by the high driving force which apparently is necessary for the nucleation of γ lamellae. A comparison with other alloys is difficult, because the formation of γ grains on slow cooling has rarely been investigated in literature [27]. The work of Takeyama et al. [28] indicates that for the alloy Ti-48Al a cooling rate below 5 K/min is necessary to obtain a considerable fraction of γ grains instead of γ lamellae. Since the cooling rate applied in the present work was more than 5 times faster, the present alloy appears to be prone to the development of γ grains. This observation agrees with the work of Pouly et al. [29] who found that γ grains developed much faster in Ti-45Al-2Nb-2Cr compared to Ti-49Al for an unknown reason.

All heat-treated specimens shown above have been subjected to an annealing treatment after the high-temperature heat treatment. As Table 1 shows high-temperature heat-treated material is far beyond the thermodynamical equilibrium and undergoes significant changes in the phase fractions during a subsequent annealing treatment at 800 or 1000 °C. The phase fractions in the different conditions have been determined by HEXRD and are shown in Table 3. For annealing at 800 °C the fraction of the α_2 phase is significantly higher and that of the β/β_0 phase is significantly lower compared to an annealing temperature of 1000 °C. To study the influence of an annealing treatment on the microstructure material was heat treated 1 h at 1270 °C, oil-quenched and annealed. In the quenched condition the microstructure exhibited mainly α_2 grains with occasionally very fine γ lamellae, γ and β grains. Subsequent annealing 6 h/800 °C/FC resulted in a microstructure that showed mainly lamellar colonies with very fine lamellae spacings, together with γ grains, and β/β_0 grains containing γ precipitates (Fig. 5). In contrast, material annealed 2 h at 1000 °C followed by furnace cooling had a pearlitic-

like microstructure of β/β_0 and γ lamellae which was observed as major constituent, besides γ and β/β_0 grains as well as lamellar ($\alpha_2 + \gamma$) colonies. This characteristic difference between annealing at 800 °C and 1000 °C was confirmed on specimens air-cooled after the heat treatment at 1270 °C (Fig. 5) which also exhibited a considerable fraction of pearlitic-like colonies. Since ($\alpha_2 + \gamma$) lamellae colonies were present before annealing the reaction $\alpha_2 + \gamma \rightarrow \gamma + \beta_0$ took place and the transformation can be designated as cellular [30]. Pearlitic/cellular microstructural morphologies have occasionally been observed in γ alloys [19, 31], e.g. after annealing at 950 °C in similar alloys as investigated in the present work [6, 17]. Here the question arises, why the phase transformation mechanisms are different at 800 °C and 1000 °C, although the constitution at these temperatures does not differ very much. A possible explanation could be that the discontinuous pearlite/cellular reaction is too slow at 800 °C to achieve an appreciable volume fraction within 6 h. According to kinetic theories of the pearlite and cellular reaction the velocity initially increases with undercooling below the eutectoid temperature, reaches a maximum at a certain temperature and drops rapidly with further decreasing temperature [32], as it is usual for nucleation and growth processes. The suggested explanation is supported by the fact that initial stages of the pearlite/cellular reaction, i.e. γ and β_0 grains at lamellar colony boundaries, were also observed in specimens that were annealed at 800 °C (Fig. 4b, c), but obviously only a small volume fraction was transformed in this manner. Accordingly the material did not achieve thermodynamic equilibrium after 6 h at 800 °C, or other processes which adapt the phase fraction, e.g. the growth of γ lamellae were faster. Wallgram et al. [17] have noted that the cellular transformation not only is driven by the chemical free energy, but also by the considerable interfacial energy stored in lamellar colonies with fine lamellae spacings, i.e. can be regarded partially as a coarsening process of lamellar colonies. For this reason the cellular transformation is promoted in alloys which are prone to precipitate fine lamellae due to additions of slowly diffusing alloying elements like Nb and Mo. In summary, the microstructure of the materials can be varied in a wider variety of morphologies as in conventional γ alloys by heat treatments. In particular, the microstructure can be significantly changed by an annealing treatment at 1000 °C due to a discontinuous reaction which transforms a considerable fraction of the material to pearlitic-like/cellular colonies.

3.4 Tensile properties and creep resistance

Tensile and creep testing was carried out to study the influence of the microstructure on the mechanical strength and to identify microstructures with an optimized combination of mechanical properties. Fig. 6 shows the influence of high-temperature heat treatment temperature on the tensile behaviour at room temperature and 700 °C. Specimens subjected to a high-temperature heat treatment at 1300 °C and exhibiting a microstructure with a 98 % fraction of lamellar colonies broke at a plastic strain below 0.5 % at room temperature and 700 °C, while plastic fracture strains > 1 % were determined at room temperature for the specimens with duplex microstructure that had been heat treated at lower temperatures (Fig. 6). This observation agrees with the common finding that the ductility of TiAl alloys with duplex microstructure is higher compared to those with fully lamellar microstructure [3, 33 – 35]. Furthermore it was found that the yield stress does not vary strongly with the high-temperature heat treatment temperature (Fig. 6) and only slightly decreased for the lowest temperature. Assuming that the lamellae spacing does not significantly differ for the three heat treatments since the same cooling rate and subsequent annealing treatment was applied, this can be ascribed to the appreciably higher fraction of equiaxed γ grains in the material heat treated at the lowest temperature. From these examinations it can be concluded that almost fully lamellar microstructures should be avoided for this alloy if ductility is of concern. Further, it appears that from the two heat treatment temperatures which generated duplex microstructures 1270 °C is preferable to 1250 °C due to the higher strength up to a temperature of 700 °C.

In a second step, the role of the cooling rate applied subsequently to the high-temperature heat treatment was investigated. As shown in Fig. 7 the yield stress rose with increasing cooling rate, whereas the plastic fracture strain significantly decreased, both at room temperature and 700 °C. The dependence of the yield strength on the cooling rate applied after the heat treatment can easily be understood by the lamellae spacing which is expected to decrease with increasing cooling rate. However, with increasing cooling rate the fraction of equiaxed γ grains is reduced and this could also slightly contribute to a higher strength. Here it should be noted that it is difficult to assess the strength properties of TiAl alloys with complex microstructures. In general, it has been found for TiAl alloys that a major part of the strength originates from internal boundaries and can be described for simple microstructures in terms of Hall-Petch relationships [36, 37], as it has been extensively discussed in ref. [5]. For duplex alloys this requires the consideration of several microstructural parameters such as the lamellae spacing, the colony and the domain size, the size of γ grains and the fractions of the

microstructural constituents. Jung et al. [38] have shown that on the basis of these parameters the overall strength of duplex alloys can reasonably well be predicted in the framework of a Hall-Petch model. As the parameters necessary were not determined here, the strength of the present materials can only be discussed qualitatively.

It was further investigated how the microstructural morphologies generated by different cooling rates after high-temperature treatment affected creep resistance. The creep curves in Fig. 8 show that the strain rate during secondary creep significantly fell with increasing cooling rate when the material was tested at 700 °C and a stress of 350 MPa. This behaviour agrees with work in literature [39 - 41], in which it is well documented that the refinement of lamellae not only improves the strength significantly but also the creep resistance. In addition, Maruyama et al. [40] have shown that the creep resistance is diminished in duplex microstructures with increasing fractions of γ grains and this could also explain the dependence on the cooling rate. As already discussed in relation with strength, it is difficult to separate the role of the different microstructural parameter with respect to mechanical properties. When creep testing was conducted at 700 °C and a lower stress of 250 MPa, the creep rate was higher for the oil-quenched and air-cooled material within the first 500 h (Fig. 8) compared to the furnace-cooled material, i.e. faster primary creep was observed for these material conditions. In literature it has been suggested that primary creep is supported by a high density of dislocations at the coherent lamellae boundaries [42, 43], but also phase transformations in lamellar materials due to non-equilibrium phase fractions and twinning could play a role [44]. In several studies it has been shown that even after annealing treatments the phase constitution of TiAl alloys continues to change during subsequent long-term ageing or creep and the microstructure correspondingly degrades [45 – 48]. This is particularly true for β -stabilized alloys in which the precipitation of the ordered β_0 phase from the α_2 phase [45, 46] as well as the precipitation of ω_0 (B8₂ structure) from α_2 or β_0 [47, 48] have been observed after long holding times at elevated temperatures. As the material conditions in which the higher cooling rates have been applied exhibit faster primary creep phase transformations may be a plausible reason for the higher primary creep rate, but an analysis of the underlying mechanisms would require additional investigations. Here it is only noted that different mechanisms govern the strain rate in the primary and secondary creep regime, which in turn depend on the microstructure of the materials. Summarizing, it can be concluded that air cooling after the high-temperature heat treatment is the optimum choice with respect to tensile and creep properties, because it enhances the yield stress and reduces

the creep strain rate for high applied stresses or long times compared to furnace-cooled material, while it improves the fracture strain in relation to oil-quenched material.

Besides the cooling rate applied after the high-temperature heat treatment the temperature of the subsequent annealing, 800 °C or 1000 °C also had a strong influence on the microstructure and therefore, its effect on tensile and creep behaviour was investigated. In Fig. 9 stress-strain curves obtained from tensile testing of differently annealed specimens are displayed. From this figure it can be seen that the annealing temperature has no big effect on the room temperature properties, but for a testing temperature of 700 °C a significant decrease of the yield stress and work hardening coefficient of the material annealed at 1000 °C was observed. It could be speculated that the latter arises due to structural changes caused by dynamic recovery, dynamic recrystallization or phase transformations, but there exists no experimental evidence for this assumption. In the creep tests it is found that the specimens annealed at 1000 °C exhibit much faster creep deformation at 700 °C and 350 MPa than those annealed at 800 °C (Fig. 10). This might also be caused by structural changes, however, the origin of this behaviour has not been studied. Again it is noted that β stabilized alloys may not be in thermodynamic equilibrium after annealing and phase transformations may occur during creep or tensile testing at elevated temperatures [45 – 48]. Since the annealing temperature of 1000 °C is significantly higher than the test or creep temperature compared to the annealing temperature of 800 °C, structural changes caused by phase transformations appear as to be a plausible explanation for the lower elevated temperature strength and creep strength of specimens annealed at 1000 °C. At lower applied stress similar strain rates were found in the primary creep regime for both annealing temperatures, while secondary creep was slower for specimens annealed at 800 °C (Fig. 10). In summary, a heat treatment comprising of holding at a temperature of 1270 °C followed by air cooling and an annealing treatment at 800 °C results in the best combination of tensile and creep properties for the alloy investigated here. As the applied temperatures are not close to single-phase regions such a treatment scheme can be reliably carried out in industrial processing. Appel et al. [5] have collected tensile data from literature determined on several γ alloys forged for ingot breakdown. Compared with this data the results obtained in the present work are excellent. This is also valid if the tensile data are compared to the alloy TNBV5 (Ti-45Al-5Nb-0.2B-0.2C, at.%) which is known for excellent tensile properties in the extruded state [5]. Compared to extruded and forged material hot-worked to a very large strain [49] the current material exhibits a yield strength and particularly a plastic fracture strain that compare favourably. The tensile data of the

present alloy is also comparable to those obtained by Wallgram et al. after forging and heat treatment on the TNM alloy which is closely related with respect to alloy composition [17]. Apparently, such data can be reproducibly achieved for forged material in this alloy class. With respect to the creep strength the minimum creep rate of the present alloy in the optimum heat treatment condition lies at the lower bound of data collected by Zhang and Deevi [44] for a test temperature of 700 °C and compares well with a K5 alloy (Ti-46.5Al-3Nb-2Cr-0.2W) in the fully lamellar condition [50]. Thus, despite the presence of the β_0 phase and a considerable fraction of γ grains a relatively high creep resistance can be attained for this alloy in the optimum heat-treated condition.

3.5 TEM investigations of crept specimens

TEM investigations of the deformation structure in the crept specimens were restricted to two specimen states: heat-treated at 1270° for 1 h followed by either air or furnace cooling and a subsequent ageing at 800 °C for 6 h. Both specimen states were crept at 700 °C with an applied load of 250 MPa to a strain of about 3 %. This took 1931 h in the case of the air-cooled and 1711 h for the furnace-cooled specimen. For the sake of brevity these specimen states will be termed furnace-cooled and air-cooled in this section. From the SEM micrographs shown in Fig. 4 c and d it is evident that the air-cooled specimen state has a lower fraction of globular γ grains and exhibits a smaller lamellae spacing. Both specimens showed bright regions in the SEM micrographs which were interpreted as β grains and are larger in the furnace-cooled specimen. In TEM these β grains in the furnace-cooled specimen showed diffraction spots corresponding with the B2 ordered β_0 variant of the β phase. Nevertheless, the grains appeared not uniform in the TEM but showed a substructure, which could not be associated with deformation structures as dislocations or twins. An example is shown in Fig. 11. Sometimes additional reflections appeared in the diffraction patterns which did not belong to the cubic B2 structure. These diffraction patterns were identified as (0001) patterns of the hexagonal ω_0 phase. From tilting experiments two orientations of the ω_0 phase were identified in the same grain with their c axes tilted by about 60° relative to each other (see Fig. 11 b and c). From dark field pictures using reflections from each of the two ω_0 orientations for imaging it is evident that the substructure present in the grain stems from domains of these two orientations located within the same grain. These domains of ω_0 phase were oriented with their respective basal (0001) planes parallel to $\{111\}$ planes of the β_0 phase in the grain. HEXRD showed that the ω_0 phase already was present prior to the creep

experiment (Table 3) although it might have grown in volume fraction during creep. It can be assumed that these finely structured β_0/ω_0 grains exhibit a high deformation resistance during creep. This could explain why the furnace-cooled specimen exhibited comparable creep strength to the air-cooled state in the test under 250 MPa load. While the higher fraction of globular γ grains and the larger lamellae spacing of the furnace-cooled specimen should cause lower creep strength the presence of significant fractions of relatively hard β_0/ω_0 grains with their fine domain substructure may compensate their effect. During the longer creep times at 250 MPa this effect could be stronger than in the tests in which 350 MPa was applied. It is debatable if β_0 grains are favourable with respect to creep strength. From nano-indentation experiments [51] it is known that the β_0 phase has a comparable mechanical strength to the α_2 phase and is superior to the γ phase at room temperature which is not surprising as all three are ordered intermetallic phases. But the situation may change at higher temperatures. While the β_0 phase should still be ordered at the creep temperature of 700 °C (which is also supported by the HEXRD results presented earlier) it is nevertheless a more open structure compared to the two close-packed α_2 and γ phases. Thus, as soon as climb or other diffusion controlled processes contribute to plastic deformation, the presence of β_0 phase should be disadvantageous. From the limited results presented here the presence of β_0/ω_0 grains seems to be beneficial for creep resistance but further investigations are necessary to clarify this point. It is noteworthy that β_0/ω_0 grains with a domain substructure as found in this work were also reported after creep testing by Schloffer et al. in an alloy with a very similar composition to the one investigated here [52]. Hence, the influence of β_0 and ω_0 phase on the creep resistance of TiAl alloys seems to be of broader interest as both phases are present to a certain amount in modern TiAl alloys with high amounts of β stabilizing alloying elements.

In the furnace-cooled specimen strong dislocation activity was detected in the γ grains. Fig. 12 shows an example of a γ grain in such a specimen with a high number of dislocations clearly visible. These dislocations were predominantly ordinary dislocations with Burger's vectors of $a/2\langle 110 \rangle$ type. While most dislocation segments observed in the γ grains are not straight but curved no obvious obstacles pinning the dislocations are visible. No in-depth analysis of slip planes and Burger's vectors was performed here but similar dislocation arrangements were associated in literature [53, 54] with a mixed climb-slip movement of dislocations.

In the lamellar colonies of the furnace-cooled specimens such dislocations were also found in the γ lamellae as shown in Fig. 13 a and a degradation of these lamellar colonies was observed. Many α_2 lamellae transform to γ phase which is evidenced from the varying

thickness and disruptions of the α_2 lamellae as well as by short remnant sections of former α_2 lamellae still embedded in the γ phase (see Fig. 13 b). The dissolution of α_2 lamellae stems from the fact that even after relatively slow furnace cooling the phase fractions in the alloy are not in thermodynamic equilibrium for 700 °C. The dissolution of the α_2 lamellae and the resulting decrease of interface density in the lamellar colonies should gradually decrease the creep resistance of the material.

The air-cooled specimen has a duplex microstructure composed of γ grains and lamellar colonies, too. Nevertheless, a striking difference when comparing with the furnace-cooled specimen is the much finer lamellae spacing in the colonies of the air-cooled material which was already observable in the SEM micrographs, Fig. 4 c and d. At higher magnification, as in the TEM micrograph shown in Fig. 14 a, it is evident that nearly no dislocation activity takes place in the γ lamellae of these colonies. This is probably due to the high Orowan stresses which have to be overcome for dislocation generation and glide in these narrow lamellae. It is striking that at a creep stress of 250 MPa the air-cooled specimen shows a faster primary creep than the furnace-cooled specimen. In the literature fast primary creep in TiAl alloys is sometimes associated with the emission of dislocations at lamellae interfaces [43, 55]. These begin to glide as soon as external load is applied and contribute to the initial deformation. This effect should be more pronounced the higher the interface density i.e. the smaller the lamellae distance. It is tempting to speculate that the high primary creep rate of the air-cooled specimen is due to its fine lamellae spacing while the creep rate decreases significantly as soon as this pool of interfacial dislocations is consumed. Nevertheless, it has to be mentioned that the effect of lamellae spacing on primary creep strain is still debated. In the literature a number of authors claim that small lamellae spacing restricts the primary creep strain [44, 56] while others found no [57] or even detrimental [58] influence of small lamellae spacing and high fractions of lamellae colonies on primary creep strain. As already discussed in the previous section phase transformations, e.g. the dissolution of α_2 lamellae due to the non-equilibrium material condition could also be the origin of the higher primary creep rate of the air-cooled material. The occurrence of γ grains in lamellae colonies of the air-cooled specimen (Fig. 14b) may indeed indicate such a transformation. However, because no TEM investigations of the primary creep stage were carried out, this needs to be confirmed. The TEM specimens investigated here stem from creep tests deformed far into the secondary creep regime. This corresponds with the absence of dislocations in the γ channels as the generation of new dislocations makes it necessary to overcome significant Orowan stresses in the narrow

lamellae while any pool of interfacial dislocations contributing to primary creep is exhausted by now.

As in the furnace-cooled specimen the γ grains show significant dislocation activity in the air-cooled material (see Fig. 14 b). The appearance of dislocations with many bowed out segments in addition to straight ones is similar, too. This fact is not surprising because both specimen states creep under similar conditions and accordingly the situation in the large γ grains should be equal leading to similar dislocation structures. Possible differences due to faster cooling, such as an excess fraction of vacancy conglomerates, which could hinder the movement of dislocations, are either not present or play a minor role.

The microstructure of the crept specimens investigated by TEM gives a number of hints to explain the differences in creep behaviour between the furnace and air-cooled states. While a larger fraction of β_0/ω_0 grains is found in the furnace-cooled specimen the air-cooled specimen exhibits much finer lamellar colonies. Fine lamellar colonies are sometimes associated with increased primary creep leading to the initially higher primary creep rates of the air-cooled alloy especially for the creep tests at 250 MPa. Generation of the relatively hard sub-structured β_0/ω_0 grains probably further contributes to the good creep resistance of the furnace-cooled specimen which is nearly up to the level of the air-cooled specimen under 350 MPa load. The superior creep strength of the air-cooled specimen becomes relevant only after longer creep times and at higher creep strains. Then dislocation generation and movement are efficiently hampered in the fine lamellar colonies of the air-cooled specimen and these colonies act as a deformation resistant microstructural constituent.

Conclusions

The phase constitution and microstructural morphology has been investigated for a TiAl alloy that has been two-step heat-treated using different heat treatment temperatures and cooling rates. It has been observed that the material significantly deviates from thermodynamic equilibrium if air cooling or faster cooling rates are applied after a high-temperature (near α transus) heat treatment. The decomposition of α is rather sluggish in the investigated material. Furthermore, the mode of the decomposition reaction depended on the cooling rate, because slower cooling not only resulted in larger lamellae spacings but also in an increased fraction of γ grains. Due to the non-equilibrium condition after a high-temperature heat-treatment

followed by air or faster cooling the subsequent annealing treatment has a strong influence on the microstructure. Annealing at 800 °C resulted in duplex microstructures while rising the annealing temperature to 1000 °C favoured the cellular reaction and transformed the major part of the material to pearlitic-like colonies.

The variations in microstructural morphology are reflected in the tensile and creep properties that varied between high strength and creep resistance together with low ductility to more ductile properties combined with lower strength levels. In the optimum condition, i.e. heat treating the material at 1270 °C followed by air cooling and annealing at 800 °C, the mechanical properties obtained compare fairly well with those of forged TNBV5 material and more conventional peritectically solidifying TiAl alloys. In detail, the creep properties cannot simply be classified by the creep strength, since primary and secondary creep do not vary in the same way with the microstructure. Furnace-cooled material exhibited low creep rates in the primary regime which was attributed to the higher thickness of γ lamellae and ω_0 precipitates, while the faster primary creep in the air-cooled material might be associated with the higher density of lamellae interfaces from which dislocation emission occurred.

Acknowledgements

The authors thank all co-workers in the PräziTal project for good cooperation, in particular S. Kötzsch, and F. Turley (Rolls-Royce Deutschland Ltd, Dahlewitz, Germany), K. Bauer-Partenheimer and P. Janschek (Leistritz Turbokomponenten GmbH, Remscheid, Germany) and V. Güther (GfE, Nürnberg, Germany). We also are grateful to U. Lorenz, S. Eggert, L. Lottermoser, D. Matthiessen and R. Kirchhof (HZG, Geesthacht) for continuous advice and support and to F. Appel (HZG, Geesthacht) for many fruitful discussions. Financial support by Rolls-Royce Deutschland Ltd and the Ministry for Economy of the Federal State Brandenburg within the Joint Project “PräziTal” is gratefully acknowledged (grant no. 80133830).

References

- [1] Tetsui T, Ono S. Composition and microstructure effects on endurance of TiAl used in turbochargers. *Intermetallics* 1999; 7: 689-697.
- [2] Bewlay BP, Weimer M, Kelly T, Suzuki A, Subramanian PR. The science, technology, and implementation of TiAl alloys in commercial aircraft engines. In: Baker I, Heilmaier M,

- Kumar S, Yoshimi K, editors. Intermetallic-Based Alloys – Science, Technology and Applications. Mater. Res. Soc. Symp. Proc. Vol. 1516. Warrendale (PA): MRS 2013, pp. 49-58.
- [3] Kim Y-W, Dimiduk DM. Designing gamma TiAl alloys: fundamentals, strategy and production. In: Nathal MV, Darolia R, Liu CT, Martin PL, Miracle DB, Wagner R, Yamaguchi M, editors. Structural Intermetallics 1997. Warrendale (PA): TMS, 1997, pp. 531-543.
- [4] Wu X. Review of alloy and process development of TiAl alloys. Intermetallics 2006; 14: 1114-1122.
- [5] Appel F, Paul JDH, Oehring M. Gamma titanium aluminide alloys – science and technology. Weinheim, Germany: Wiley-VCH, 2011.
- [6] Clemens H, Mayer S. Design, processing, microstructure, and applications of advanced intermetallic TiAl alloys. Adv. Eng. Mater. 2013; 15: 191-215.
- [7] Naka S, Thomas M, Sanchez C, Khan T. Development of third generation castable gamma titanium aluminides: role of solidification paths. In: Nathal MV, Darolia R, Liu CT, Martin PL, Miracle DB, Wagner R, Yamaguchi M, editors. Structural Intermetallics 1997. Warrendale (PA): TMS, 1997, pp. 313-322.
- [8] Küstner V, Oehring M, Chatterjee A, Güther V, Brokmeier H-G, Clemens H, Appel F. An investigation of microstructure formation during solidification of gamma titanium aluminide alloys. In: Kim Y-W, Clemens H, Rosenberger AH, editors. Gamma Titanium Aluminides 2003. Warrendale (PA): TMS, 2003, pp. 89-96.
- [9] Jin Y, Wang JN, Yang J, Wang Y. Microstructure refinement of cast TiAl alloys by β solidification. Scripta Mater. 2004; 52: 113-117.
- [10] Imayev RM, Imayev VM, Oehring M, Appel F. Alloy design concepts for refined gamma titanium aluminide based alloys. Intermetallics 2007; 15: 451-460.
- [11] Clemens H, Wallgram W, Kremmer S, Güther V, Otto A, Bartels A. Design of novel β -solidifying TiAl alloys with adjustable β /B2-phase fraction and excellent hot-workability. Adv. Eng. Mater. 2008; 10: 707-713.
- [12] Kim Y-W, Kim S-L, Dimiduk D, Woodward C. Development of beta gamma alloys: opening robust processing and greater application potential for TiAl-base alloys. In: Kim Y-W, Morris D, Yang R, Leyens C, editors. Structural Aluminides for Elevated Temperatures. Warrendale (PA): TMS, 2008, p. 215.
- [13] Hu D, Jiang H, Wu X. Microstructure and tensile properties of cast Ti-44Al-4Nb-4Hf-0.1Si-0.1B alloy with refined microstructures. Intermetallics 2009; 17: 744-748.

- [14] Lindemann J, Glavatskikh M, Leyens C, Roth-Fagaraseanu D. Effect of small boron and carbon additions on the mechanical properties of a novel high niobium containing gamma titanium aluminide alloy. In: Kim Y-W, Morris D, Yang R, Leyens C, editors. Structural Aluminides for Elevated Temperatures. Warrendale (PA): TMS, 2008, pp. 257-264.
- [15] Tetsui T, Shindo K, Kobayashi S, Takeyama M. A newly developed hot worked TiAl alloy for blades and structural components. *Scripta Mater.* 2002; 47: 399-403.
- [16] Tetsui T, Shindo K, Kaji S, Kobayashi S, Takeyama M. Fabrication of TiAl components by means of hot forging and machining. *Intermetallics* 2005; 13: 971-978.
- [17] Wallgram W, Schmölder T, Cha L, Das G, Güther V, Clemens H. Technology and mechanical properties of advanced γ -TiAl based alloys. *Int. J. Mat. Res. (Z. Metallkd.)* 2009; 100: 1021-1030.
- [18] Stark A, Oehring M, Pyczak F, Schreyer A. In situ observation of various phase transformations in Nb-rich TiAl alloys during quenching with different rates. *Adv. Eng Mater.* 2011, 13: 700-704.
- [19] Appel F, Oehring M, Paul JDH. Nano-Scale design of TiAl alloys based on β -phase decomposition. *Adv. Eng. Mater.* 2006, 8:371-376.
- [20] Staron P, Fischer T, Lippmann T, Stark A, Daneshpour S, Schnubel D, Uhlmann E, Gerstenberger R, Camin B, Reimers W, Eidenberger E, Clemens H, Huber N, Schreyer A. In situ experiments with synchrotron high-energy x-rays and neutrons. *Adv. Eng. Mater.* 2011; 13: 658-663.
- [21] Lutterotti L, Bortolotti M, Ischia G, Lonardelli I, Wenk H-R. Rietveld texture analysis from diffraction images. *Z. Krist. Suppl.* 2007, 26: 125-130.
- [22] Nobuki M, Tsujimoto T. Influence of alloy composition on hot deformation properties of Ti-Al binary intermetallics. *ISIJ (Iron and Steel Institute of Japan) International* 1991; 31:931-937.
- [23] Semiatin SL, Chesnutt JC, Austin C, Seetharaman V. Processing of intermetallic alloys. In: Nathal MV, Darolia R, Liu CT, Martin PL, Miracle DB, Wagner R, Yamaguchi M, editors. *Structural Intermetallics 1997*. Warrendale (PA): TMS, 1997, pp. 263-276.
- [24] Imayev RM, Imayev VM, Oehring M, Appel F. Microstructural evolution during hot working of Ti aluminide alloys: influence of phase constitution and initial casting texture. *Metall. Mater. Trans. A* 2005; 36A 859-867.
- [25] Semiatin SL, Seetharaman V, Weiss I. Hot workability of titanium and titanium aluminide alloys – an overview. *Mater. Sci. Eng. A* 1998; A243: 1-24.

- [26] Witusiewicz VT, Bondar, AA, Hecht U, Velikanova TYa. The Al-B-Nb-Ti system IV. Experimental study and thermodynamic re-evaluation of the binary Al-Nb and ternary Al-Nb-Ti systems. *J. Alloys Comp.* 2009; 472: 133-161.
- [27] Ramanujan RV. Phase transformations in γ -based titanium aluminides. *Intern. Mater. Rev.* 2000; 45: 217-240.
- [28] Takeyama M, Kumagai T, Nakamura M, Kikuchi M. Cooling rate dependence of the α_2/γ phase transformation in titanium aluminides and its application to alloy development. In: Darolia R, Lewandowski JJ, Liu CT, Martin PL, Miracle DB, Nathal MV, editors. *Structural Intermetallics 1993*. Warrendale (PA): TMS, 1993, pp. 167-176.
- [29] Pouly P, Hua M-J, Garcia CI, DeArdo AJ. Isothermal transformation behaviour of near- γ TiAl alloys. *Scripta Metall. Mater.* 1993; 29: 1529-1534.
- [30] Aaronson HI, Enomoto M, Lee JK. Mechanisms of diffusional phase transformations in metals and alloys. Boca Baton, FL: CRC Press, 2010.
- [31] Zhang Z, Leonard KJ, Dimiduk DM, Vasudevan VK. Phase transformations and microstructure evolution in multicomponent gamma titanium aluminides. In: Hemker KJ, Dimiduk DM, Clemens H, Darolia R, Inui H, Larsen JM, Sikka VK, Thomas M, Whittenberger JD, editors. *Structural Intermetallics 2001*. Warrendale (PA): TMS, 2001, p. 515-526.
- [32] Doherty RD. Diffusive phase transformations in the solid state. In: Cahn RW, Haasen P, editors. *Physical metallurgy, vol. II*. Amsterdam (The Netherlands): North-Holland Physics Publishing, 1983, pp. 933-1030.
- [33] Huang S-C, Hall EL. Plastic deformation and fracture of binary TiAl-Base alloys. *Metall. Trans. A* 1991; 22A: 427-439.
- [34] Kim Y-W. Microstructural evolution and mechanical properties of a forged gamma titanium aluminide alloy. *Acta Metall. Mater.* 1992; 40: 1121-1134.
- [35] Yamaguchi M, Inui H. TiAl compounds for structural applications. In: Darolia R, Lewandowski JJ, Liu CT, Martin PL, Miracle DB, Nathal MV, editors. *Structural Intermetallics*. Warrendale (PA): TMS, 1993, pp. 127-142.
- [36] Vasudevan VK, Court SA, Kurath P, Fraser HL. Effect of grain size and temperature on the yield stress of the intermetallic compound TiAl. *Scripta Metall.* 1989; 23:467-469.
- [37] Umakoshi Y, Nakano T. The role of ordered domains and slip mode of α_2 phase in the plastic behaviour of TiAl crystals containing oriented lamellae. *Acta Metall. Mater.* 1993; 41: 1155-1161.

- [38] Jung JY, Park JK, Chun CH, Her SM. Hall-Petch relation in two-phase TiAl alloys. *Mater. Sci. Eng. A* 1996; A220: 185-190.
- [39] Crofts PD, Bowen P, Jones IP. The effect of lamella thickness on the creep behaviour of Ti-48Al-2Nb-2Mn. *Scripta Mater.* 1996, 35: 1391.
- [40] Maruyama K, Yamamoto R, Nakakuki H, Fujitsuna N. Effects of lamellar spacing, volume fraction and grain size on creep strength of fully lamellar alloys. *Mater. Sci. Eng. A* 1997; A239-240: 419-428.
- [41] Parthasarathy TA, Mendiratta MG, Dimiduk DM. Observations on the creep behaviour of fully-lamellar polycrystalline TiAl: identification of critical effects. *Scripta Mater.* 1997; 37: 315-321.
- [42] Es-Souni M, Bartels A, Wagner R. Creep behaviour of a fully transformed near γ -TiAl alloy Ti-48Al-2Cr. *Acta Metall. Mater.* 1995; 43: 153-161.
- [43] Appel F, Christoph U. Coherency stresses and interface-related deformation phenomena in two-phase titanium aluminides. *Intermetallics* 1999; 7: 1173-1182.
- [44] Zhang WJ, Deevi SC. The controlling factors in primary creep rate of TiAl-base alloys. *Intermetallics* 2003; 11: 177-185.
- [45] Du X-W, Zhu J, Zhang X, Cheng ZY, Kim Y-W. Creep-induced $\alpha_2 \rightarrow \beta_2$ phase transformation in a fully-lamellar TiAl alloy. *Scripta Mater.* 2000; 43: 597-602.
- [46] Wang JG, Nieh TG. Creep of a β phase-containing TiAl alloy. *Intermetallics* 2000; 8: 737-748.
- [47] Huang, ZW. Ordered ω phases in a 4Zr-4Nb-containing TiAl-based alloy. *Acta Mater.* 2008; 56: 1689-1700.
- [48] Lapin J, Pelachová T, Witusiewicz VT, Dobročka E. Effect of long-term ageing on microstructure stability and lattice parameter of coexisting phases in intermetallic Ti-46Al-8Ta alloy. *Intermetallics* 2011; 19: 121-124.
- [49] Paul JDH, Lorenz U, Oehring M, Appel F. Up-scaling the size of TiAl components made via ingot metallurgy. *Intermetallics* 2013; 32: 318-328.
- [50] Kim Y-W, Schwenker SW. The creep behaviour of gamma alloy Ti-46.5Al-3Nb-2Cr-0.2W (Alloy K5) in two microstructural conditions. In: Kim Y-W, Wagner R, Yamaguchi M, editors. *Gamma Titanium Aluminides*. Warrendale (PA): TMS, 1995, pp. 985-992.
- [51] Schloffer M, Iqbal F, Gabrisch H, Schwaighofer E, Schimansky F-P, Mayer S, Stark A, Lippmann T, Göken M, Pyczak F, Clemens H. Microstructure development and hardness of a powder metallurgical multiphase γ -TiAl based alloy. *Intermetallics* 2012; 22: 231-240.

- [52] Schloffer M, Rashkova B, Schöberl T, Schwaighofer E, Zhang Z, Clemens H, Mayer S. Evolution of the ω_0 phase in a β -stabilized multi-phase TiAl alloy and its effect on hardness. *Acta Mater.* 2014; 64: 241–252.
- [53] Malaplate J, Caillard D, Couret A. Interpretation of the stress dependence of creep by a mixed climb mechanism in TiAl. *Phil. Mag.* 2004; 84: 3671–3687.
- [54] Malaplate J, Thomas M., Belaygue P, Grange M, Couret A. Primary creep at 750 °C in two cast and PM Ti48Al48Cr2Nb2 alloys. *Acta Mater.* 2006; 54: 601–611.
- [55] Chen WR, Beddoes J, Zhao L. Effect of aging on the tensile and creep behaviour of a fully lamellar near γ -TiAl alloy. *Mater. Sci. Eng. A* 2002; 323: 306–317.
- [56] Parthasarathy TA, Keller M, Mendiratta MG. The effect of lamellar lath spacing on the creep behaviour of Ti-47at% Al. *Scripta Mater.* 1998; 38: 1025–1031.
- [57] Beddoes J, Seo DY, Chen WR, Zhao L. Relationship between tensile and primary creep properties of near γ -TiAl intermetallics. *Intermetallics* 2001; 9: 915–922.
- [58] Es-Souni M, Bartels A, Wagner R, Creep behaviour of near γ -TiAl base alloys: effects of microstructure and alloy composition. *Mater. Sci. Eng. A* 1995, 192/193: 698-706.

Condition	Phase fraction (%)		
	α_2 (D0 ₁₉)	γ (L1 ₀)	β/β_o (A2/B2)
1 h/1270 °C/oil quenching	68	30	2
1 h/1270 °C/oil quenching + 6 h/800 °C/furnace cooling	19	79	2
1 h/1270 °C/oil quenching + 2 h/1000 °C/furnace cooling	6	83	11

Table 1. Phase fractions as determined by HEXRD and Rietveld refinement. The specimens had been extruded, forged and then subjected to the given heat treatments.

Condition	Fraction of microstructural constituent (%)		
	Lamellar ($\alpha_2 + \gamma$) Colonies	β/β_0 grains	equiaxed γ grains
1 h/1250 °C/air cooling + 6 h/800 °C/furnace cooling	55.8 ± 3.8	8.4 ± 0.8	35.8 ± 3.1
1 h/1270 °C/furnace cooling + 6 h/800 °C/furnace cooling	23.5 ± 2.1	15.2 ± 1.2	61.4 ± 0.9
1 h/1270 °C/air cooling + 6 h/800 °C/furnace cooling	72.8 ± 1.0	3.6 ± 0.1	23.7 ± 0.9
1 h/1270 °C/oil quenching + 6 h/800 °C/furnace cooling	84.9 ± 1.9	2.3 ± 0.1	12.9 ± 2.0
1 h/1300 °C/air cooling + 6 h/800 °C/furnace cooling	98.1 ± 0.7	1.9 ± 0.7	0

Table 2. Microstructural constituent fractions as determined from scanning electron micrographs. The specimens had been forged and then subjected to the given heat treatment.

Condition	Phase fraction (%)			
	γ	α_2	β/ω	ω variant
1 h/1250 °C/air cooling + 6 h/800 °C/furnace cooling	77.3	15.3	7.3	ω''
1 h/1270 °C/furnace cooling + 6 h/800 °C/furnace cooling	81.0	9.6	9.4	ω_o
1 h/1270 °C/air cooling + 6 h/800 °C/furnace cooling	77.0	18.4	4.6	-
1 h/1270 °C/oil quenching + 6 h/800 °C/furnace cooling	78.4	18.7	2.9	-
1 h/1300 °C/air cooling + 6 h/800 °C/furnace cooling	81.9	15.6	2.5	-
1 h/1270 °C/air cooling + 2 h/1000 °C/furnace cooling	83.4	6.7	9.9	ω''
1 h/1270 °C/oil quenching + 2 h/1000 °C/furnace cooling	82.6	6.1	11.4	ω''

Table 3. Phase fractions as determined by HEXRD and Rietveld refinement. The specimens had been forged and then subjected to the given heat treatments. ω_o : ordered ω -phase with $B8_2$ structure, ω'' : trigonal ω -phase, spacegroup P -3 m1.

Figure captions

Fig. 1. Scanning electron micrographs taken in the back-scattering electron mode after casting and HIPing (a, b) and after subsequent forging in the $(\alpha + \gamma + \beta)$ phase field (c). The long axis of the cast piece was perpendicular to the image plane in (a) and (b), while the forging direction lies vertically in (c). The arrows in (c) indicate bent lamellae.

Fig. 2. Results of a DSC investigation of forged material (a) and a HEXRD heating study of extruded and forged material (b), (c), both at a heating rate of 20 K/min. (b) Integrated intensity of Bragg reflections (in grey scale) after integrating azimuthally over the Debye-Scherrer rings that were recorded during heating to 1400 °C. On the y axis the scattering vector q is displayed and on the x axis the temperature which is common for all three diagrams (a) – (c). (c) Phase fractions of the three phases α , β and γ in the ordered (α_2 , β_0) or disordered state (left axis) and relative intensity of superlattice reflections of the α_2 and β_0 phases related to a temperature of 1000 °C (right axis).

Fig. 3. Scanning electron micrographs taken in the back-scattering electron mode of forged specimens that were heat treated for 1 h at (a) 1250 °C, (b) 1270 °C and (c) 1300 °C. Subsequently the samples were air-cooled and then annealed 6 h at 800 °C.

Fig. 4. Scanning electron micrographs taken in the back-scattering electron mode of forged specimens that were heat treated for 1 h at 1270 °C and oil-quenched (a), (b), air-cooled (c) or furnace-cooled (d). Subsequently the samples were annealed for 6 h at 800 °C. The arrows in (b) indicate region where γ and β/β_0 grains were formed at colony boundaries (1) and a β/β_0 grain in which γ lamellae were precipitated (2). The inset in (c) shows a detailed high magnification image in which the initial stage of the cellular transformation can be seen to start at a colony boundary.

Fig. 5. Scanning electron micrographs taken in the back-scattering electron mode of forged specimens that were heat treated for 1 h at 1270 °C and oil-quenched (a), (b), or air-cooled (c), (d). Subsequently the samples were annealed 6 h at 800 °C (a), (c) or 2h at 1000 °C (b), (d).

Fig. 6. Tensile test stress-strain curves obtained at room temperature (a) and 700 °C (b) from specimens that were heat treated for 1 h at the temperature indicated in the diagrams followed by air cooling and 6 h annealing at 800 °C.

Fig. 7. Tensile test stress-strain curves obtained at room temperature (a) and 700 °C (b) from specimens that were heat treated for 1 h at 1270 °C followed by cooling with the indicated rate and 6 h annealing at 800 °C.

Fig. 8. Creep curves obtained by testing at 700 °C and an initial load of 350 MPa (a) or 250 MPa (b). The specimens were heat treated for 1 h at 1270 °C followed by cooling with the indicated rate and 6 h annealing at 800 °C.

Fig. 9. Tensile test stress-strain curves obtained at room temperature (a) and 700 °C (b) from specimens that were heat treated for 1 h at 1270 °C followed by air cooling and subsequently annealed as indicated.

Fig. 10. Creep curves obtained by testing at 700 °C and an initial load of 350 MPa (a) or 250 MPa (b). The specimens were heat treated for 1 h at 1270 °C followed by air cooling and subsequently annealed as indicated.

Fig. 11. (a) Bright field TEM micrograph of a ω_0 grain; (b) the same particle pictured in dark field imaging using the reflection marked in the insert; (c) same particle pictured after tilting the specimen by about 60° using the reflection marked in the insert. The specimen had been heat treated for 1 h at 1270 °C followed by furnace-cooling, annealed for 6 h at 800 °C and then creep tested at 700 °C under an initial load of 250 MPa up to a strain of 3.0 %.

Fig. 12. Dislocation structure in a γ grain imaged by TEM using a $1\bar{1}1$ two beam condition; the grain is oriented near the 110 orientation. The specimen was heat treated for 1 h at 1270 °C followed by furnace-cooling, annealed for 6 h at 800 °C and then creep tested at 700 °C under an initial load of 250 MPa up to a strain of 3.0 %.

Fig. 13. TEM micrographs of lamellar colonies in the furnace-cooled and creep-deformed specimen; (a) showing dislocations in a number of γ lamellae; (b) showing remnants of

dissolving α_2 lamellae. The specimen was heat treated for 1 h at 1270 °C followed by furnace-cooling and 6 h annealing at 800 °C and then creep deformed at 700 °C using an initial load of 250 MPa up to a strain of 3.0 %.

Fig. 14. Microstructure of the air-cooled and creep-deformed specimen; (a) lamellar colony; (b) γ -grain with dislocations oriented along the 110 zone axis pictured using a $\bar{1}1\bar{1}$ two beam condition. The specimen was heat treated for 1 h at 1270 °C followed by air-cooling and 6 h annealing at 800 °C and then creep deformed at 700 °C using an initial load of 250 MPa up to a strain of 2.8 %.

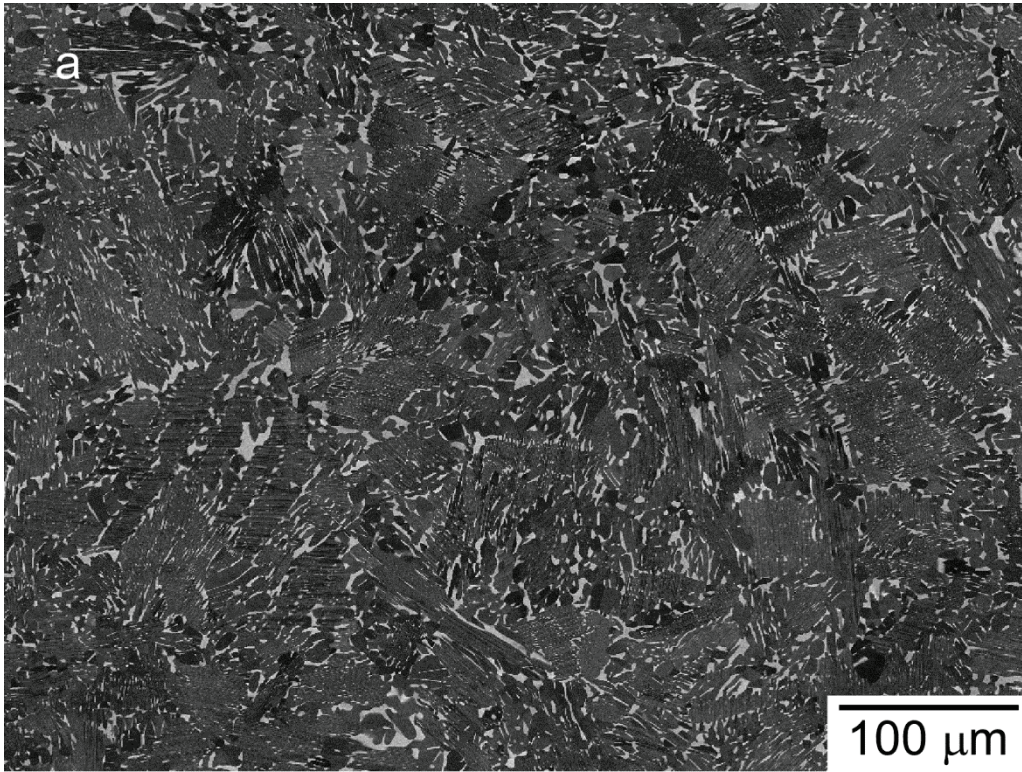


Fig. 1. Scanning electron micrographs taken in the back-scattering electron mode after casting and HIPing (a), (b) and (c) after subsequent forging in the $(\alpha + \gamma + \beta)$ phase field. The long axis of the cast piece was perpendicular to the image plane in (a) and (b), while the forging direction lies vertically (c). The arrows in (c) indicate bent lamellae.

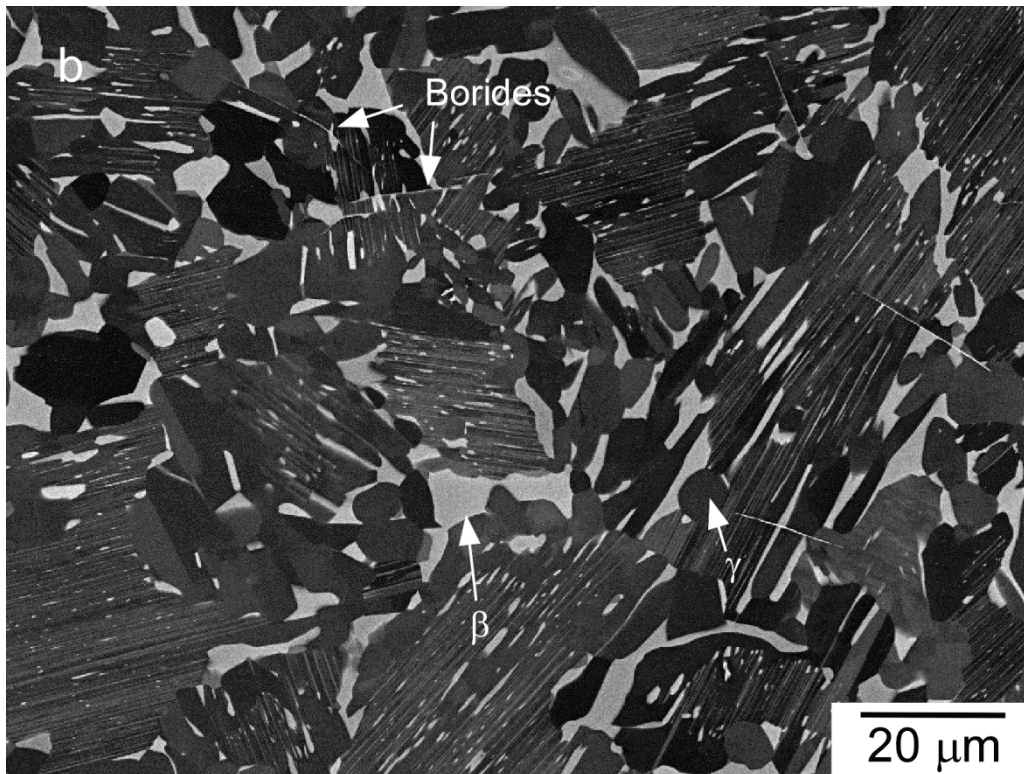


Fig. 1. Scanning electron micrographs taken in the back-scattering electron mode after casting and HIPing (a), (b) and (c) after subsequent forging in the $(\alpha + \gamma + \beta)$ phase field. The long axis of the cast piece was perpendicular to the image plane in (a) and (b), while the forging direction lies vertically (c). The arrows in (c) indicate bent lamellae.

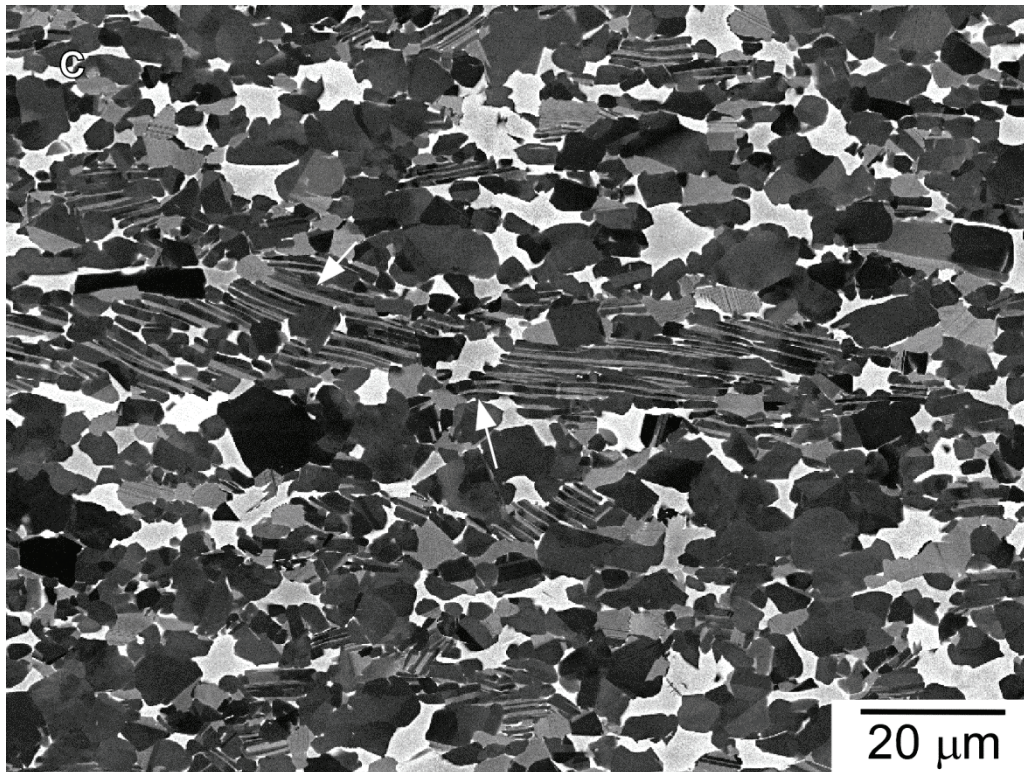


Fig. 1. Scanning electron micrographs taken in the back-scattering electron mode after casting and HIPing (a), (b) and (c) after subsequent forging in the $(\alpha + \gamma + \beta)$ phase field. The long axis of the cast piece was perpendicular to the image plane in (a) and (b), while the forging direction lies vertically (c). The arrows in (c) indicate bent lamellae.

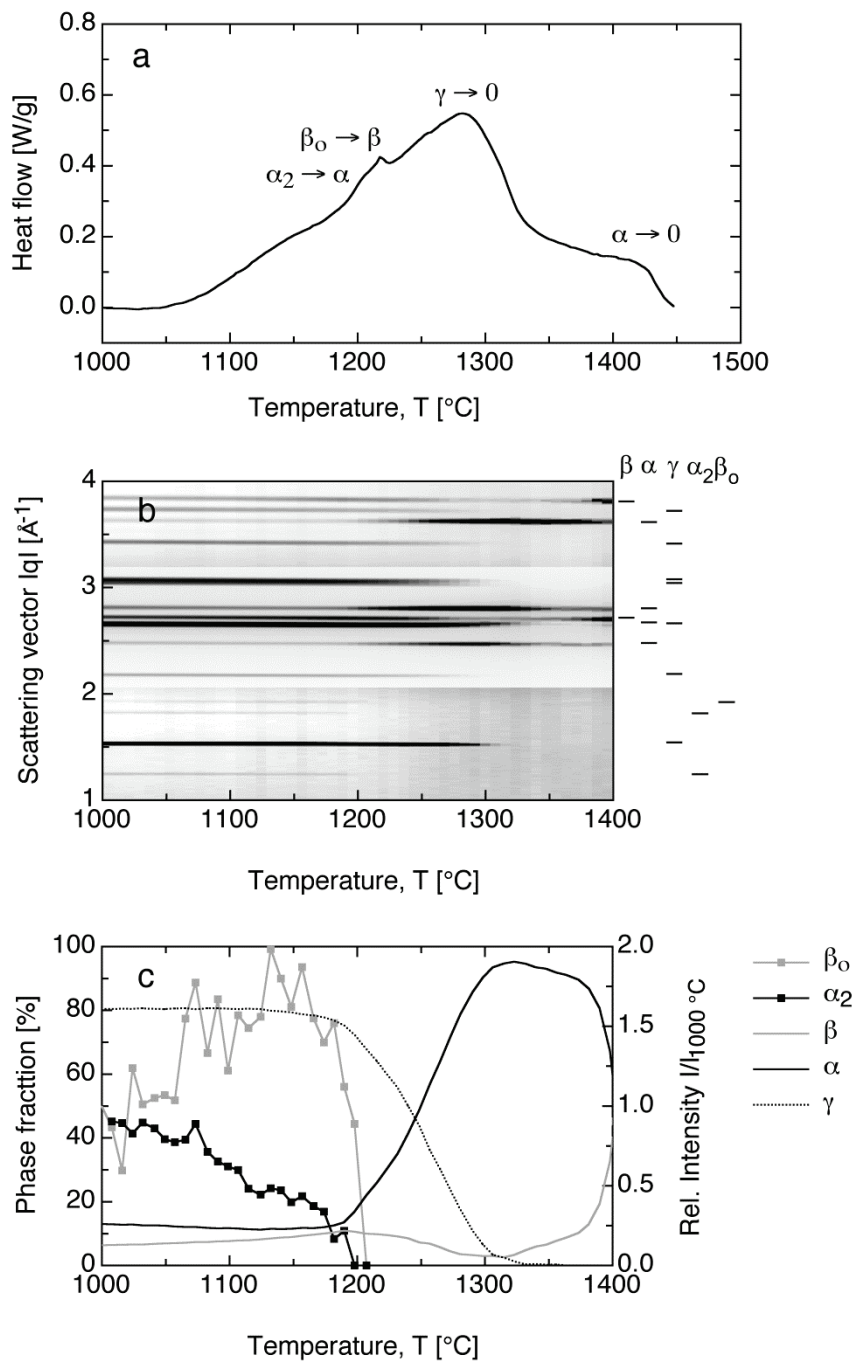


Fig. 2. Results of a DSC investigation of forged material (a) and a HEXRD heating study of extruded and forged material (b), (c), both at a heating rate of 20 K/min. (b) Integrated intensity of Bragg reflections (in grey scale) after integrating azimuthally over the Debye-Scherrer rings that were recorded during heating to 1400 °C. On the y axis the scattering vector q is displayed and on the x axis the temperature which is common for all three diagrams (a) – (c). (c) Phase fractions of the three phases α , β and γ in the ordered (α_2 , β_0) or

disordered state (left axis) and relative intensity of superlattice reflections of the α_2 and β_0 phases related to a temperature of 1000 °C (right axis).

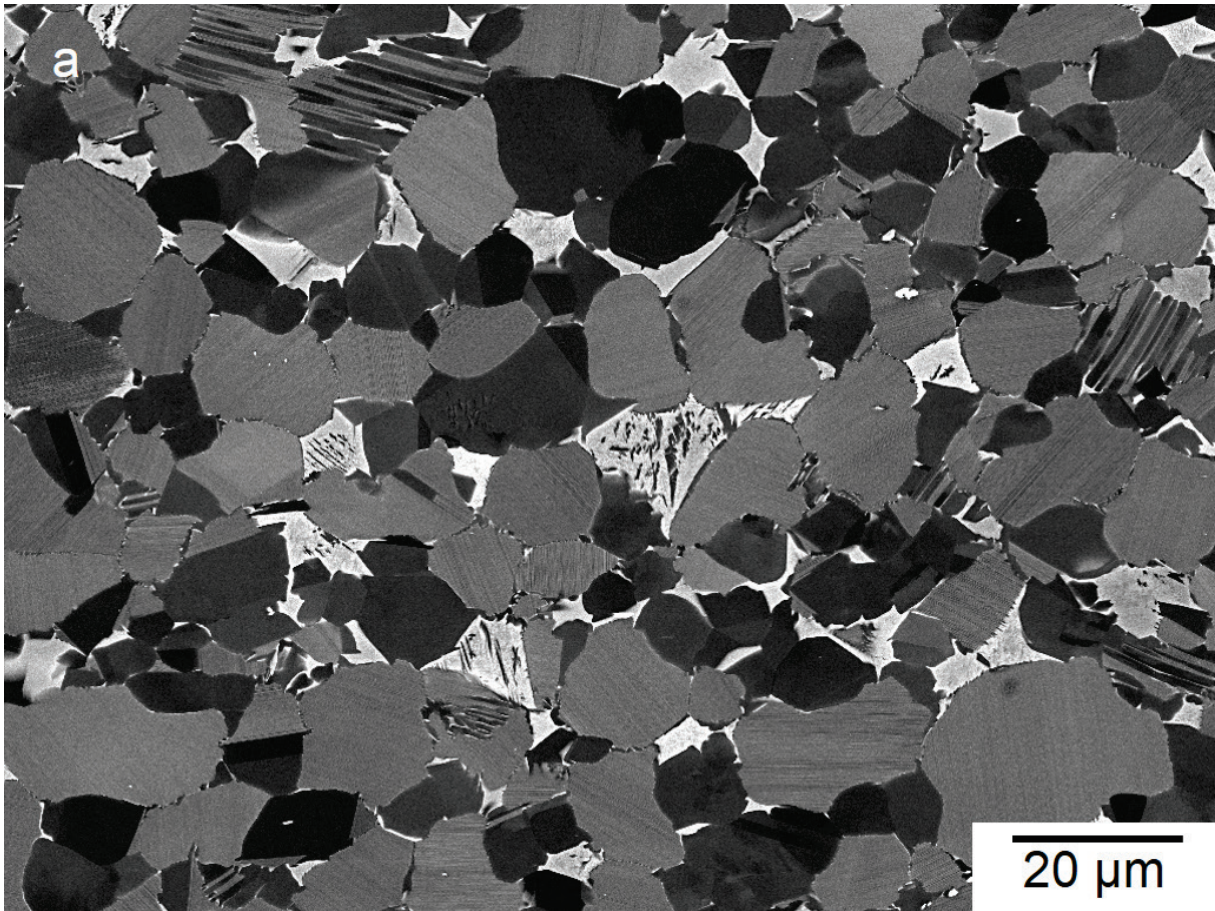


Fig. 3. Scanning electron micrographs taken in the back-scattering electron mode of forged specimens that were heat treated for 1 h at (a) 1250 °C, (b) 1270 °C and (c) 1300 °C. Subsequently the samples were air-cooled and then annealed 6 h at 800 °C.

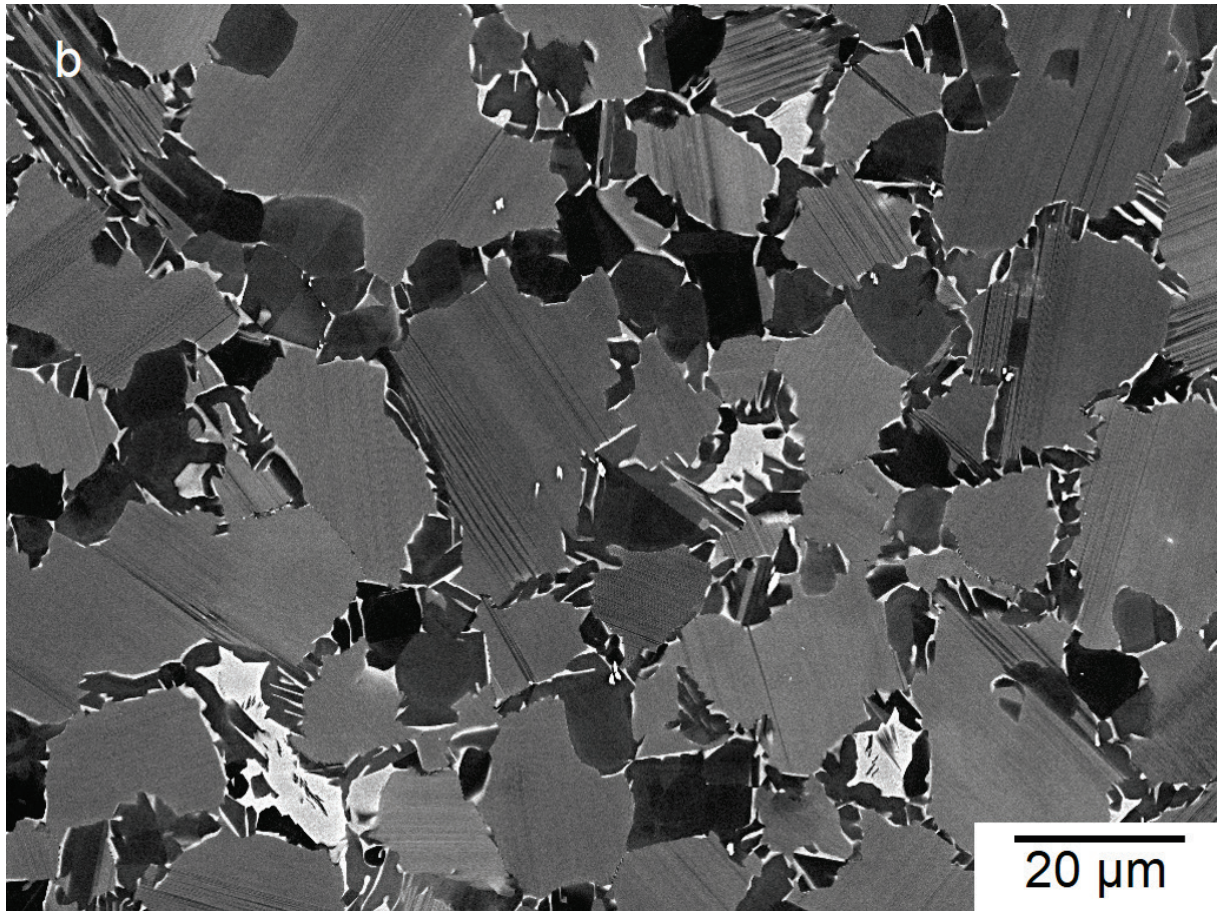


Fig. 3. Scanning electron micrographs taken in the back-scattering electron mode of forged specimens that were heat treated for 1 h at (a) 1250 °C, (b) 1270 °C and (c) 1300 °C. Subsequently the samples were air-cooled and then annealed 6 h at 800 °C.

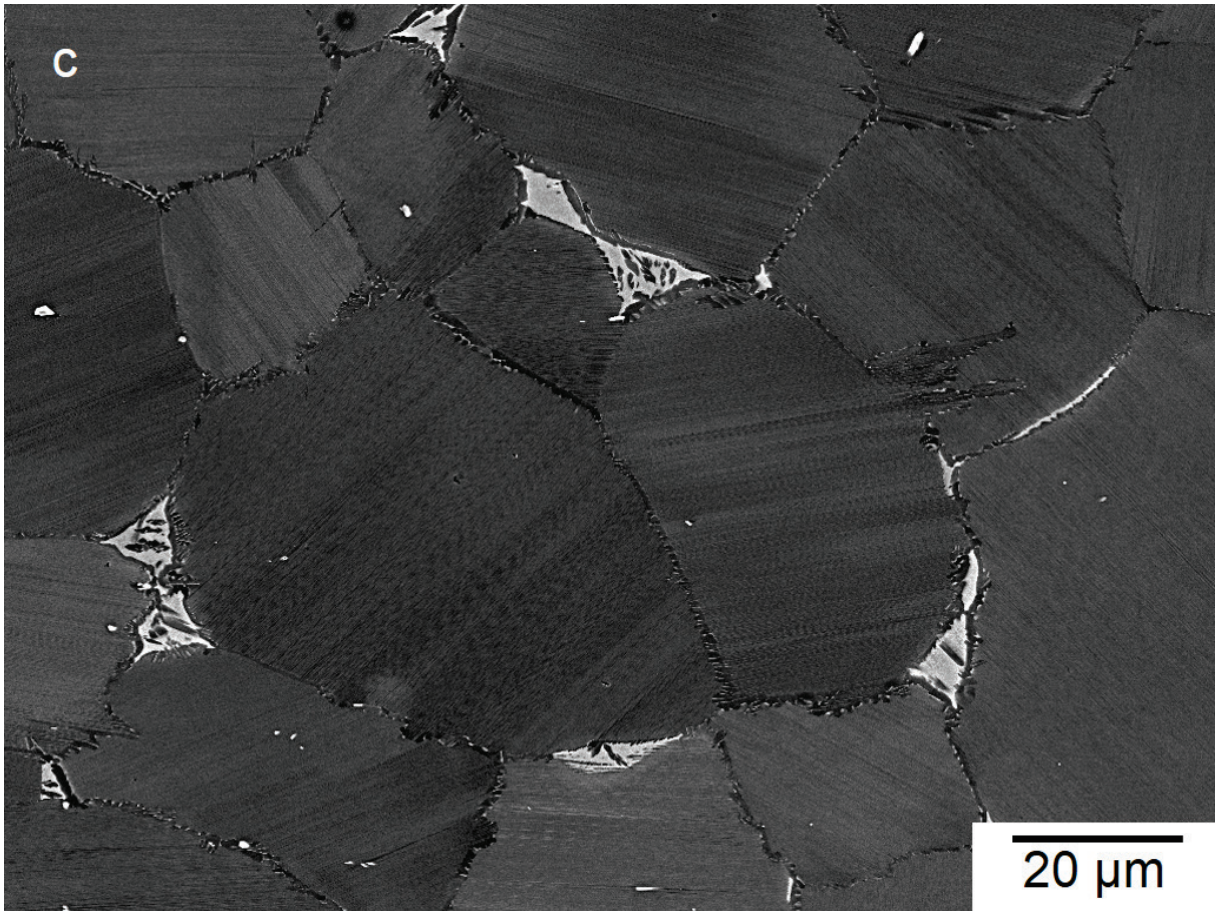


Fig. 3. Scanning electron micrographs taken in the back-scattering electron mode of forged specimens that were heat treated for 1 h at (a) 1250 °C, (b) 1270 °C and (c) 1300 °C. Subsequently the samples were air-cooled and then annealed 6 h at 800 °C.

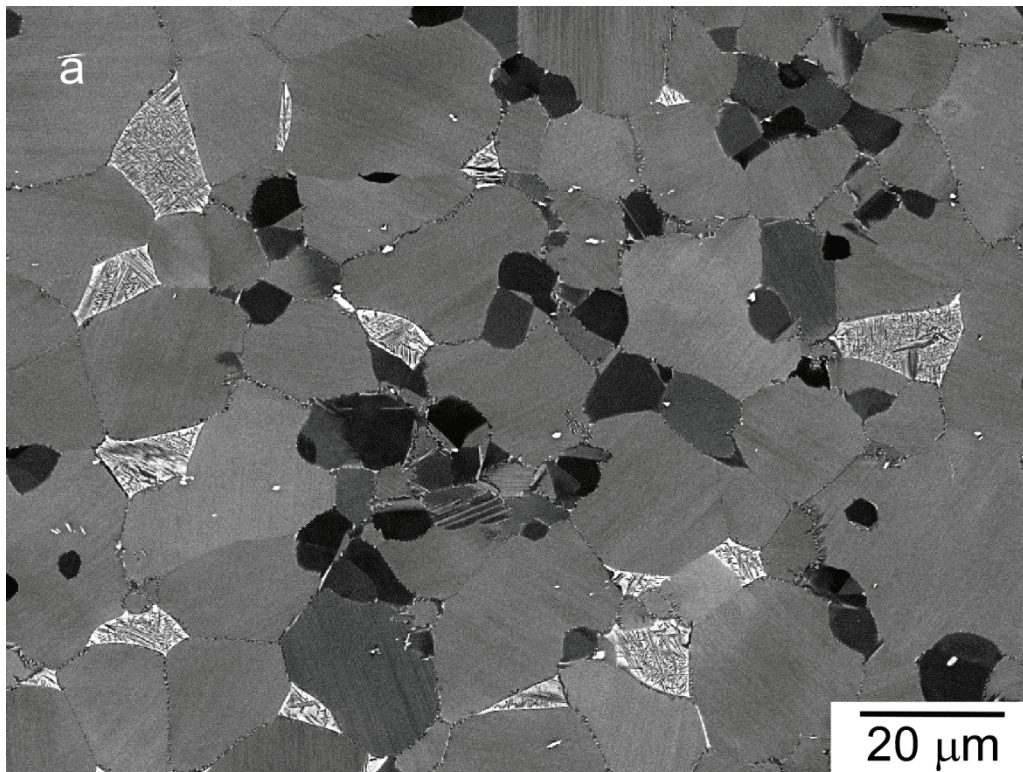


Fig. 4. Scanning electron micrographs taken in the back-scattering electron mode of forged specimens that were heat treated for 1 h at 1270 °C and oil-quenched (a), (b), air-cooled (c) or furnace-cooled (d). Subsequently the samples were annealed for 6 h at 800 °C. The arrows in (b) indicate region where γ and β/β_0 grains were formed at colony boundaries (1) and a β/β_0 grain in which γ lamellae were precipitated (2). The inset in (c) shows a detailed high magnification image in which the initial stage of the cellular transformation can be seen to start at a colony boundary.

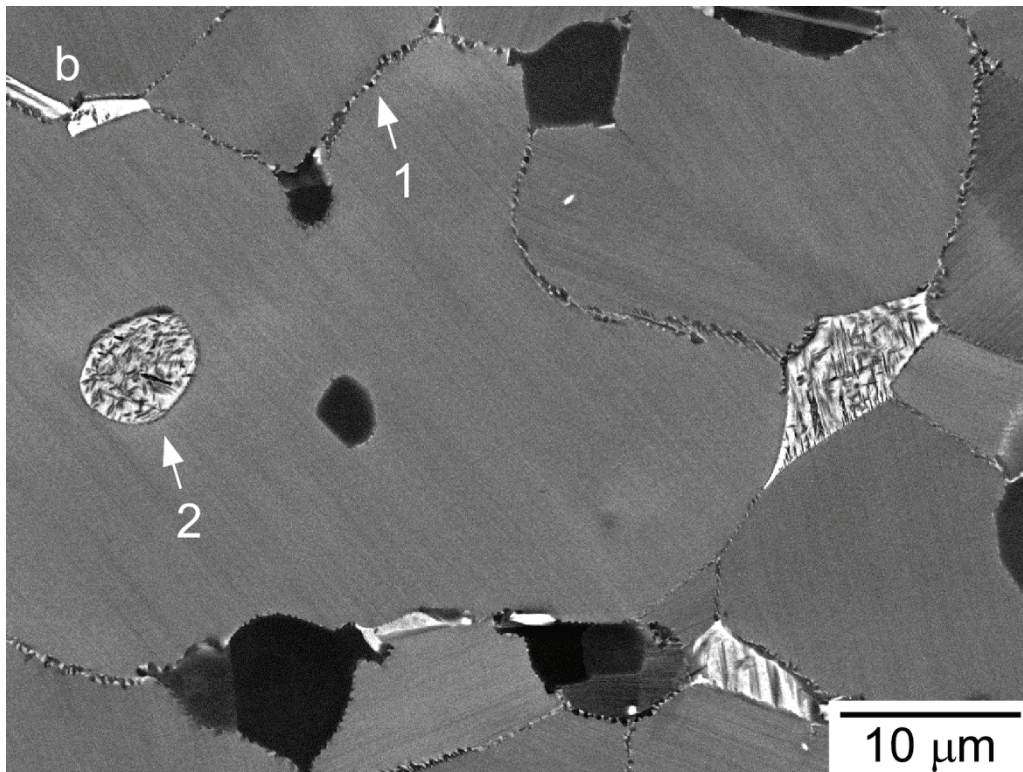


Fig. 4. Scanning electron micrographs taken in the back-scattering electron mode of forged specimens that were heat treated for 1 h at 1270 °C and oil-quenched (a), (b), air-cooled (c) or furnace-cooled (d). Subsequently the samples were annealed for 6 h at 800 °C. The arrows in (b) indicate region where γ and β/β_0 grains were formed at colony boundaries (1) and a β/β_0 grain in which γ lamellae were precipitated (2). The inset in (c) shows a detailed high magnification image in which the initial stage of the cellular transformation can be seen to start at a colony boundary.

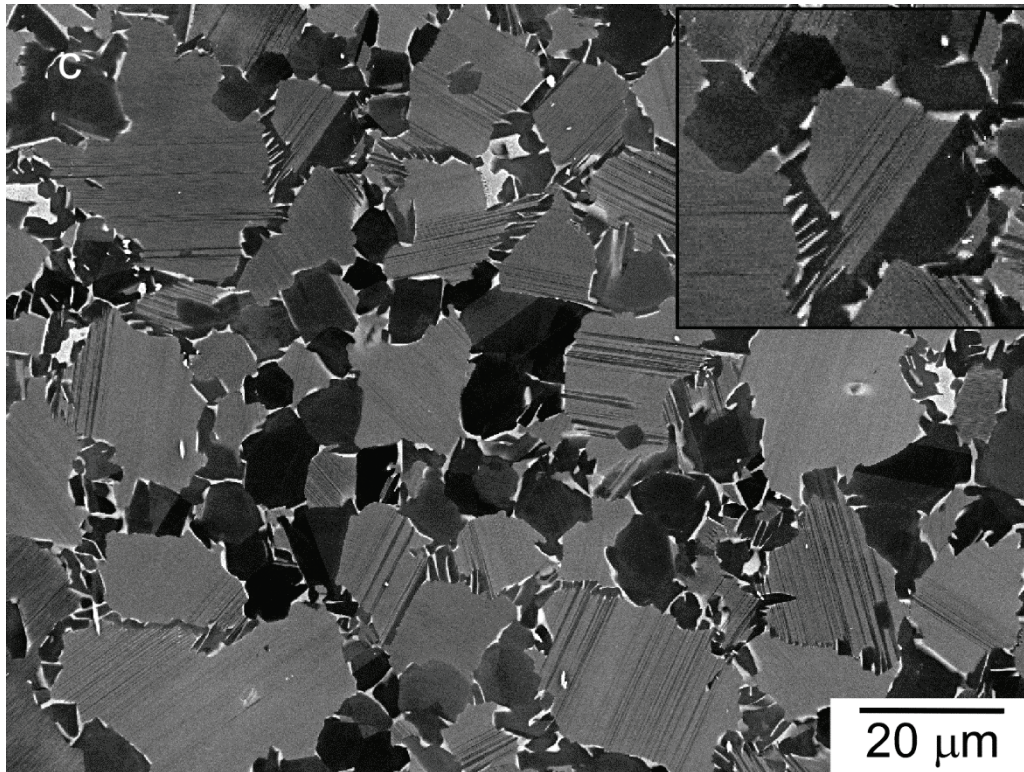


Fig. 4. Scanning electron micrographs taken in the back-scattering electron mode of forged specimens that were heat treated for 1 h at 1270 °C and oil-quenched (a), (b), air-cooled (c) or furnace-cooled (d). Subsequently the samples were annealed for 6 h at 800 °C. The arrows in (b) indicate region where γ and β/β_0 grains were formed at colony boundaries (1) and a β/β_0 grain in which γ lamellae were precipitated (2). The inset in (c) shows a detailed high magnification image in which the initial stage of the cellular transformation can be seen to start at a colony boundary.

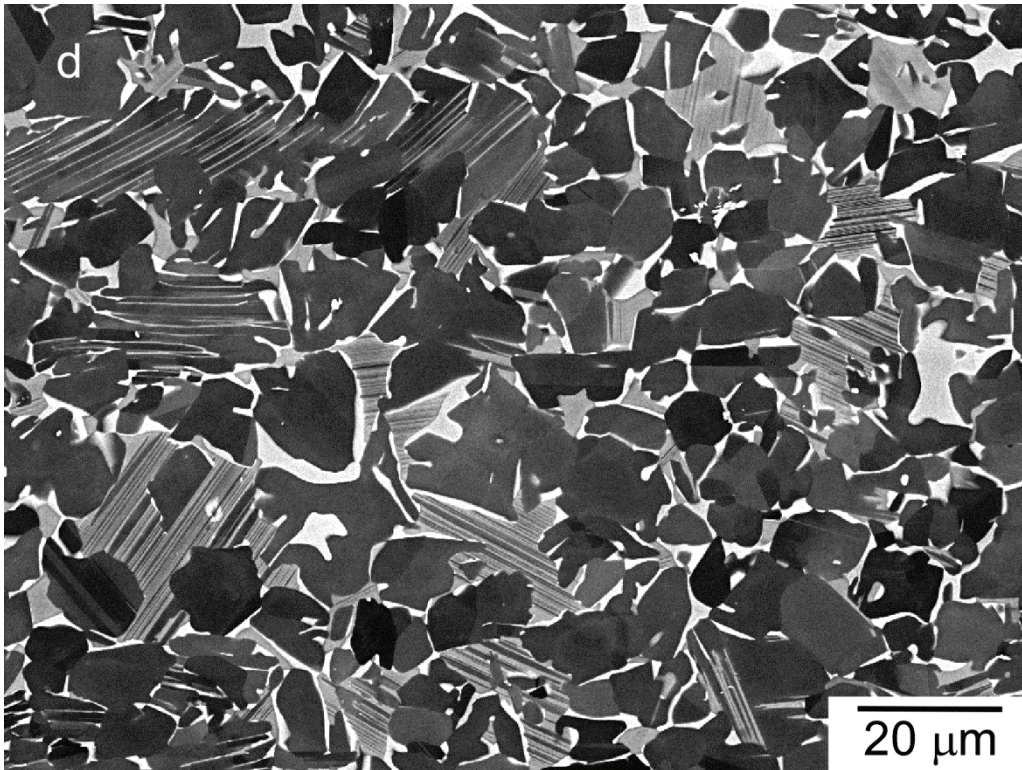


Fig. 4. Scanning electron micrographs taken in the back-scattering electron mode of forged specimens that were heat treated for 1 h at 1270 °C and oil-quenched (a), (b), air-cooled (c) or furnace-cooled (d). Subsequently the samples were annealed for 6 h at 800 °C. The arrows in (b) indicate region where γ and β/β_0 grains were formed at colony boundaries (1) and a β/β_0 grain in which γ lamellae were precipitated (2). The inset in (c) shows a detailed high magnification image in which the initial stage of the cellular transformation can be seen to start at a colony boundary.

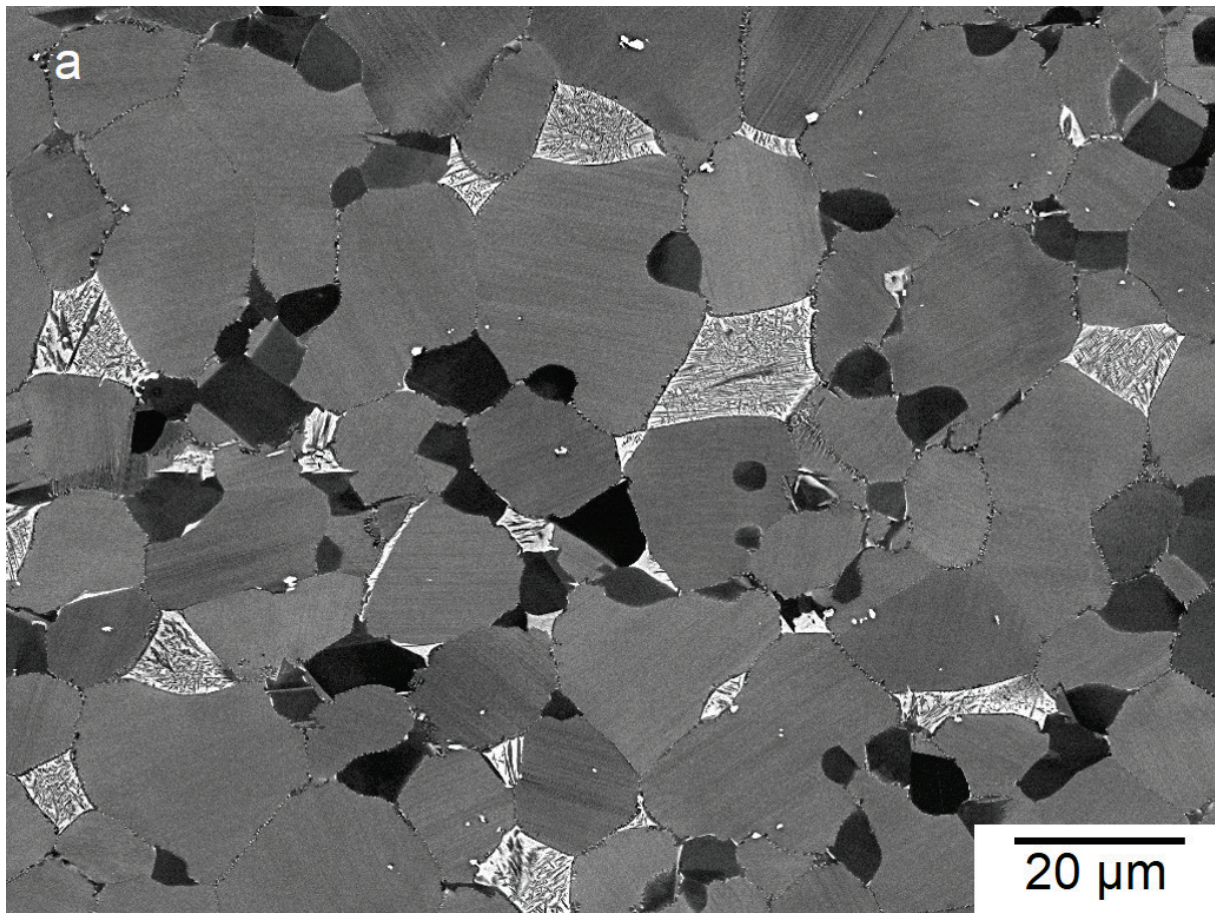


Fig. 5. Scanning electron micrographs taken in the back-scattering electron mode of forged specimens that were heat treated for 1 h at 1270 °C and oil-quenched (a), (b), or air-cooled (c), (d). Subsequently the samples were annealed 6 h at 800 °C (a), (c) or 2h at 1000 °C (b), (d).

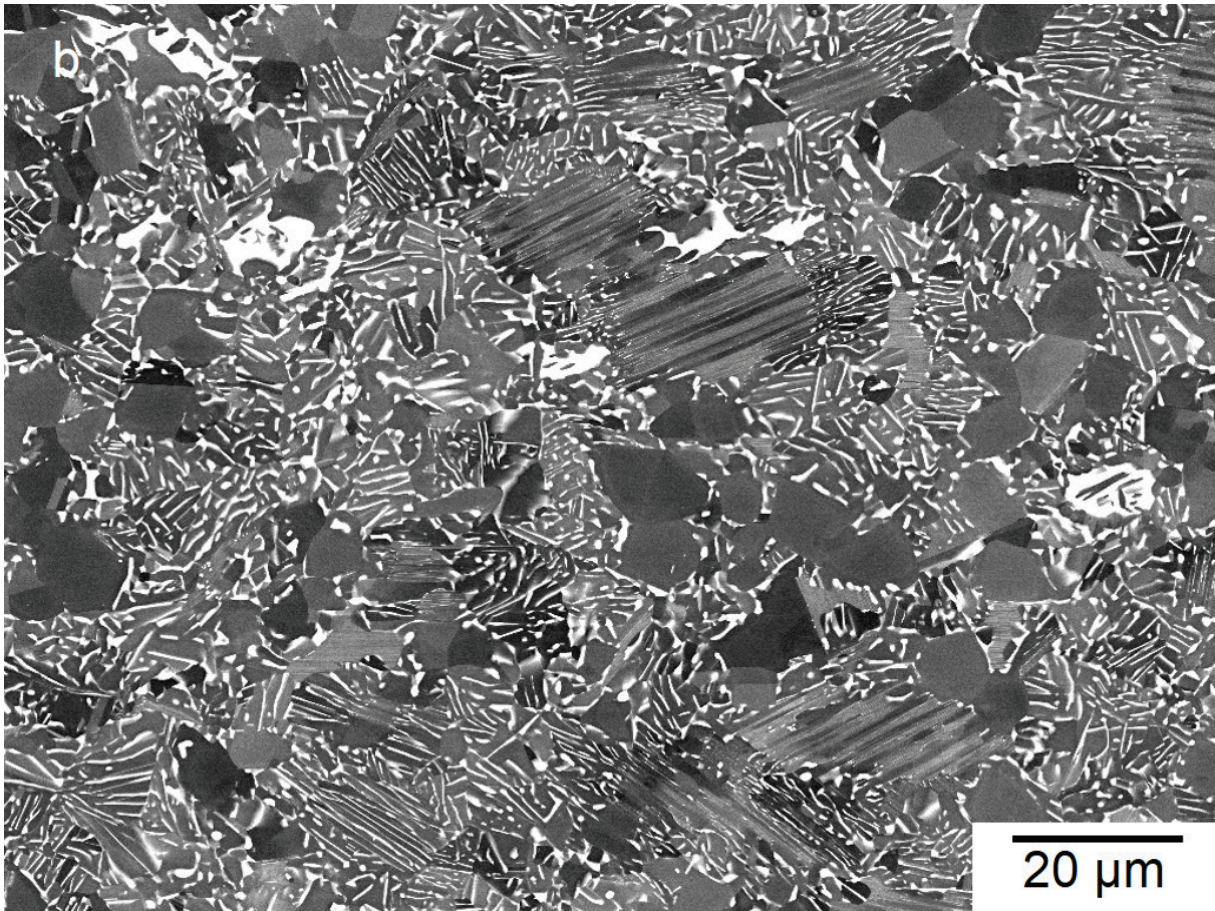


Fig. 5. Scanning electron micrographs taken in the back-scattering electron mode of forged specimens that were heat treated for 1 h at 1270 °C and oil-quenched (a), (b), or air-cooled (c), (d). Subsequently the samples were annealed 6 h at 800 °C (a), (c) or 2h at 1000 °C (b), (d).

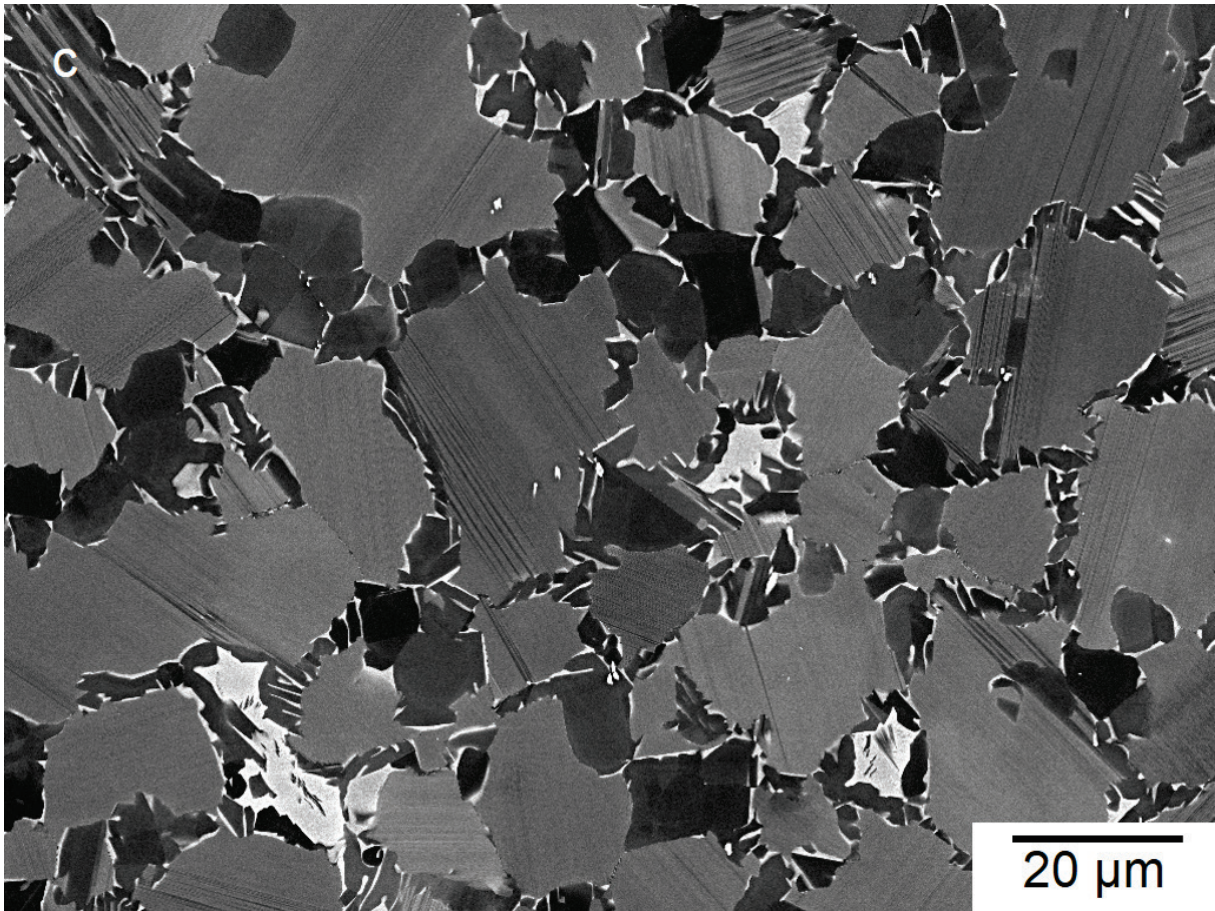


Fig. 5. Scanning electron micrographs taken in the back-scattering electron mode of forged specimens that were heat treated for 1 h at 1270 °C and oil-quenched (a), (b), or air-cooled (c), (d). Subsequently the samples were annealed 6 h at 800 °C (a), (c) or 2h at 1000 °C (b), (d).

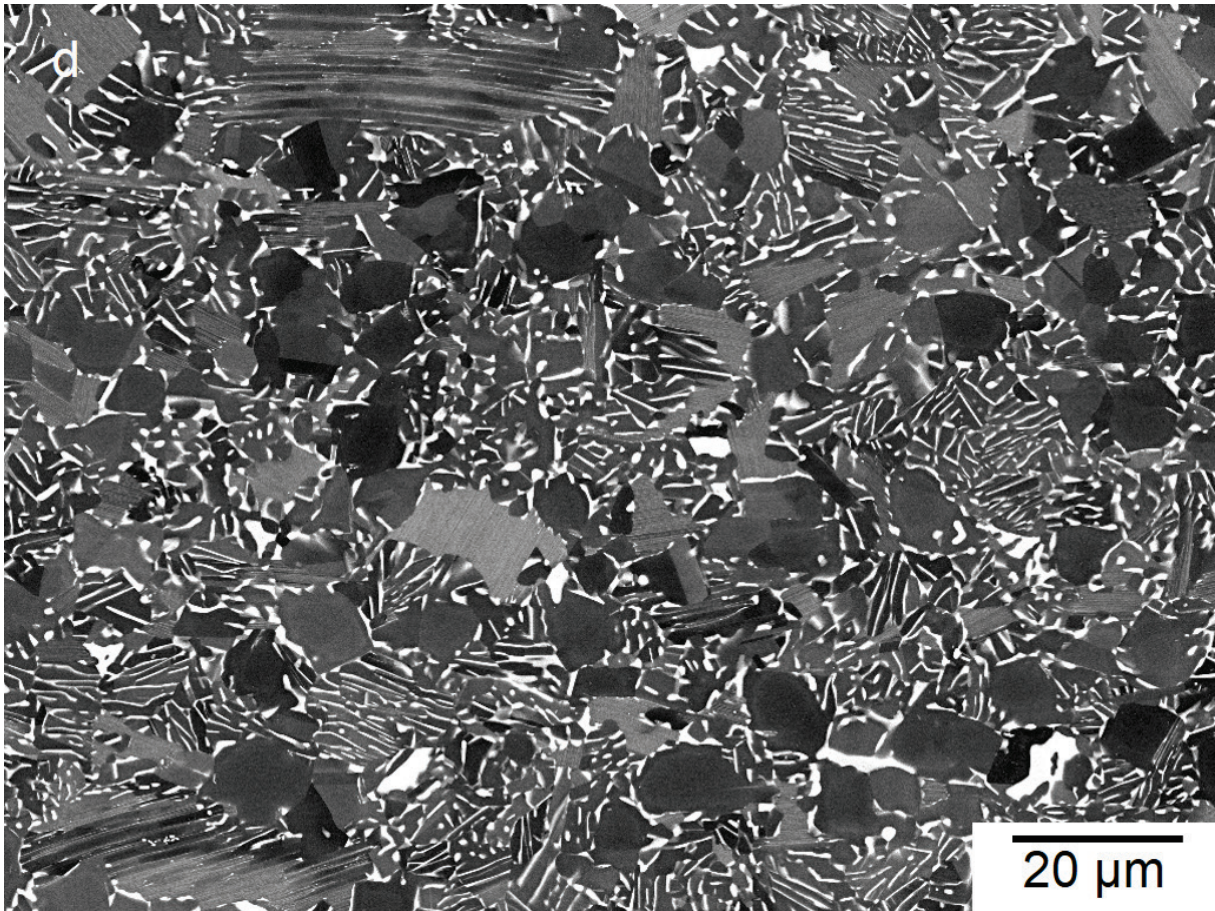


Fig. 5. Scanning electron micrographs taken in the back-scattering electron mode of forged specimens that were heat treated for 1 h at 1270 °C and oil-quenched (a), (b), or air-cooled (c), (d). Subsequently the samples were annealed 6 h at 800 °C (a), (c) or 2h at 1000 °C (b), (d).

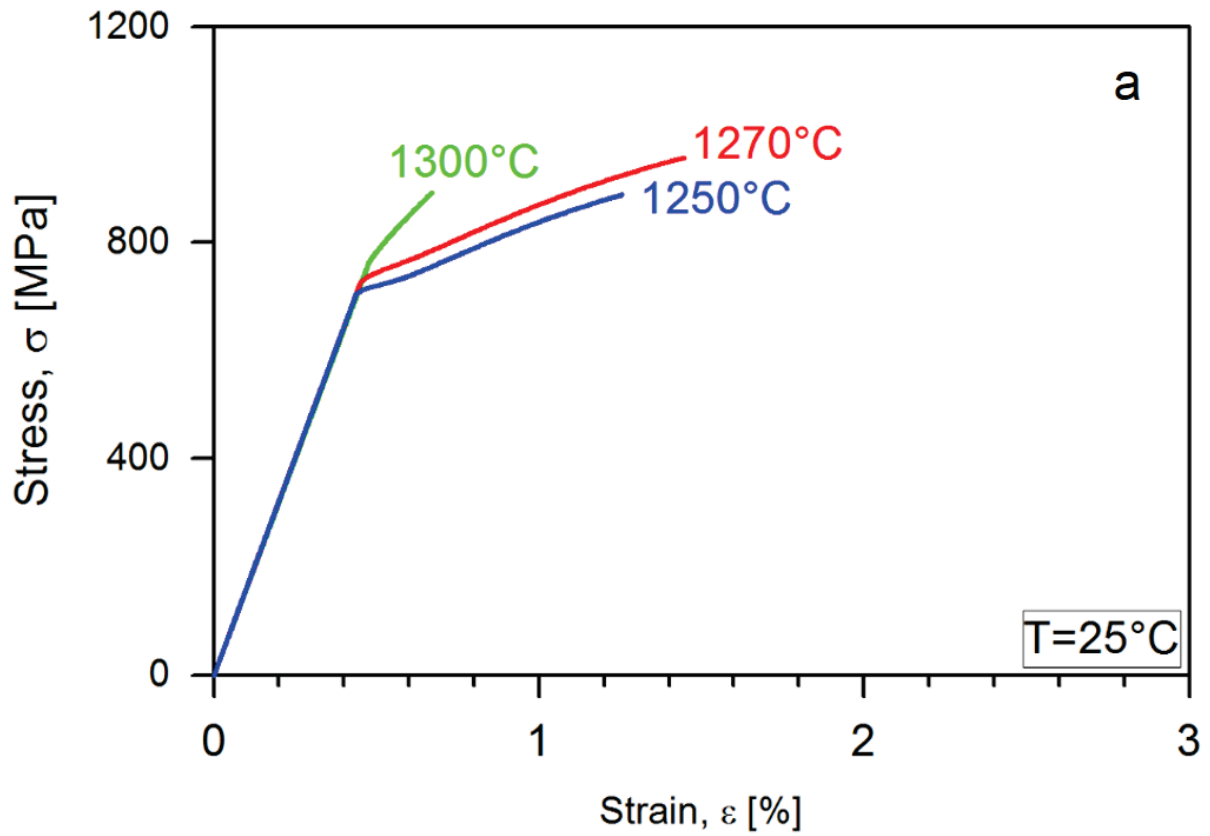


Fig. 6. Tensile test stress-strain curves obtained at room temperature (a) and 700 °C (b) from specimens that were heat treated for 1 h at the temperature indicated in the diagrams followed by air cooling and 6 h annealing at 800 °C.

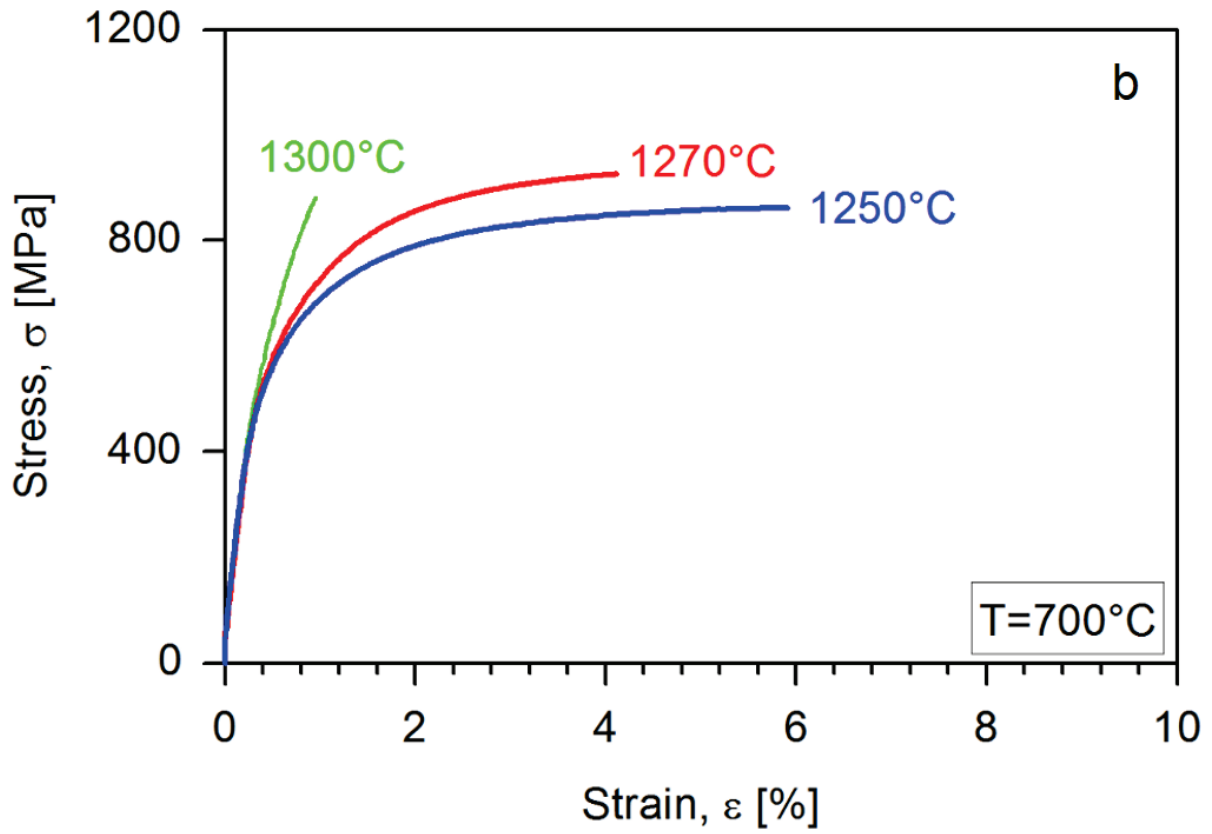


Fig. 6. Tensile test stress-strain curves obtained at room temperature (a) and 700 °C (b) from specimens that were heat treated for 1 h at the temperature indicated in the diagrams followed by air cooling and 6 h annealing at 800 °C.

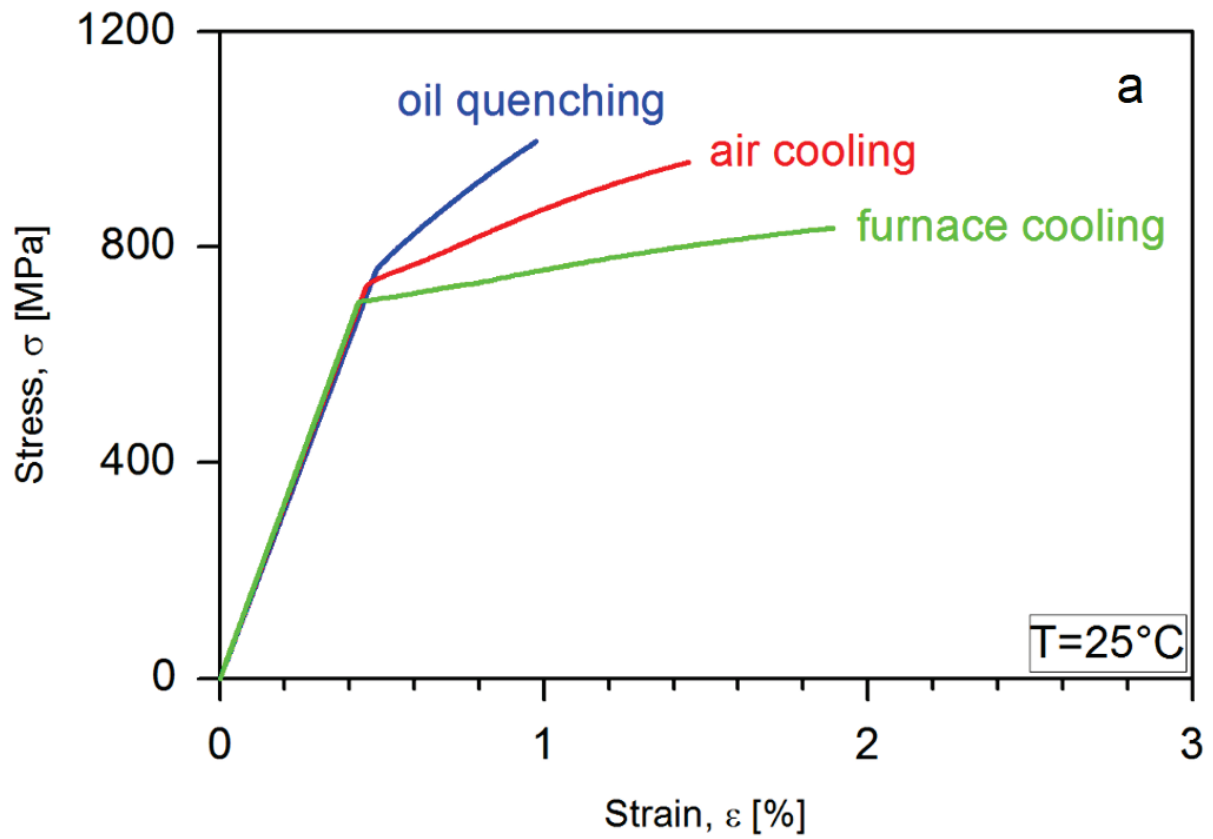


Fig. 7. Tensile test stress-strain curves obtained at room temperature (a) and 700 °C (b) from specimens that were heat treated for 1 h at 1270 °C followed by cooling with the indicated rate and 6 h annealing at 800 °C.

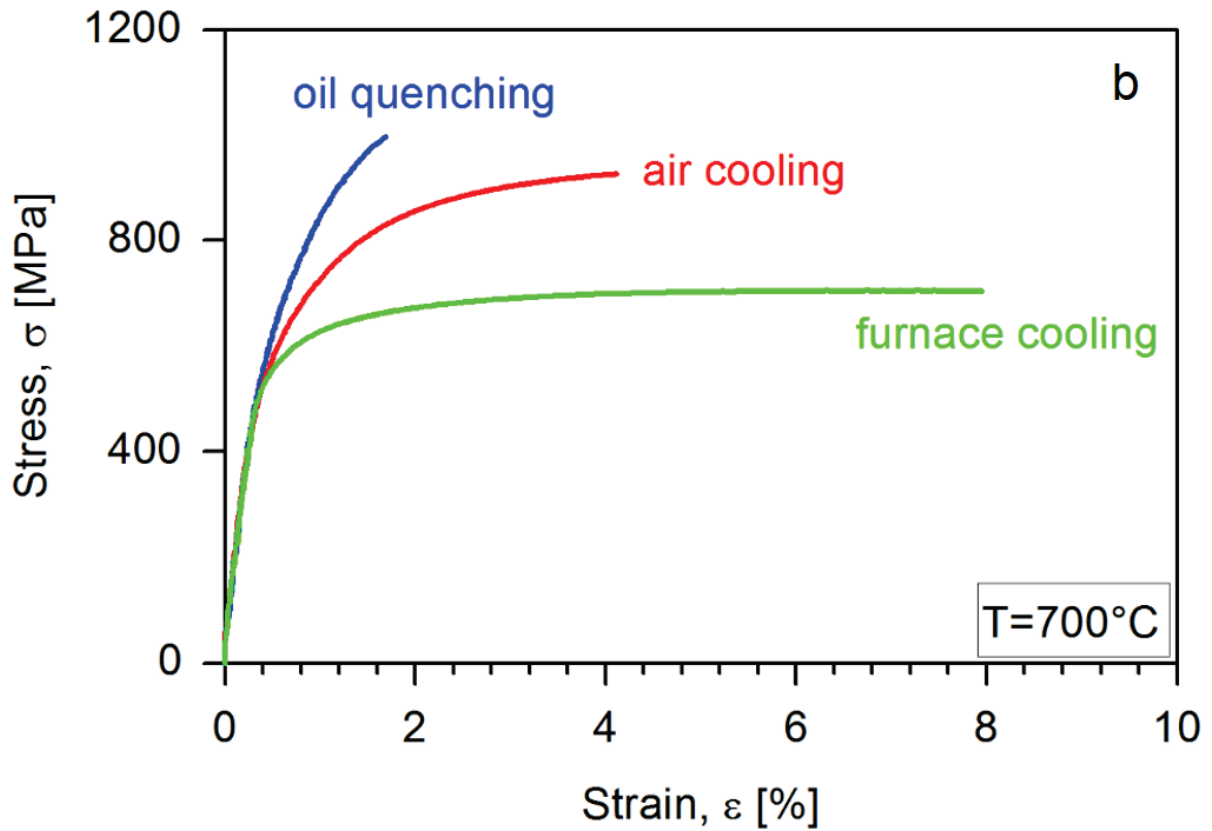


Fig. 7. Tensile test stress-strain curves obtained at room temperature (a) and 700 °C (b) from specimens that were heat treated for 1 h at 1270 °C followed by cooling with the indicated rate and 6 h annealing at 800 °C.

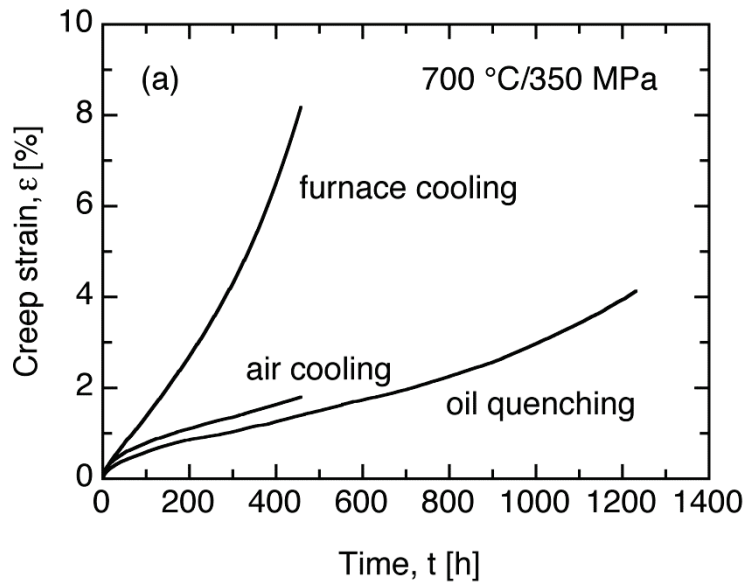


Fig. 8. Creep curves obtained by testing at 700 °C and an initial load of 350 MPa (a) or 250 MPa (b). The specimens were heat treated for 1 h at 1270 °C followed by cooling with the indicated rate and 6 h annealing at 800 °C.

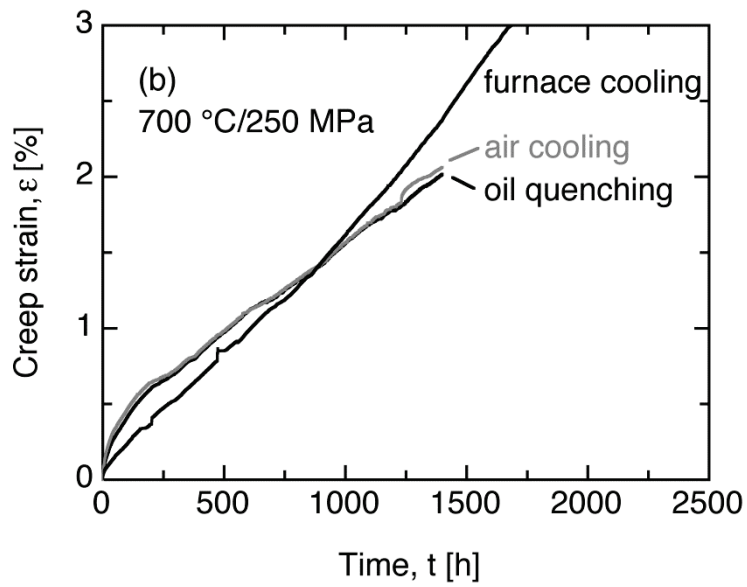


Fig. 8. Creep curves obtained by testing at 700 °C and an initial load of 350 MPa (a) or 250 MPa (b). The specimens were heat treated for 1 h at 1270 °C followed by cooling with the indicated rate and 6 h annealing at 800 °C.

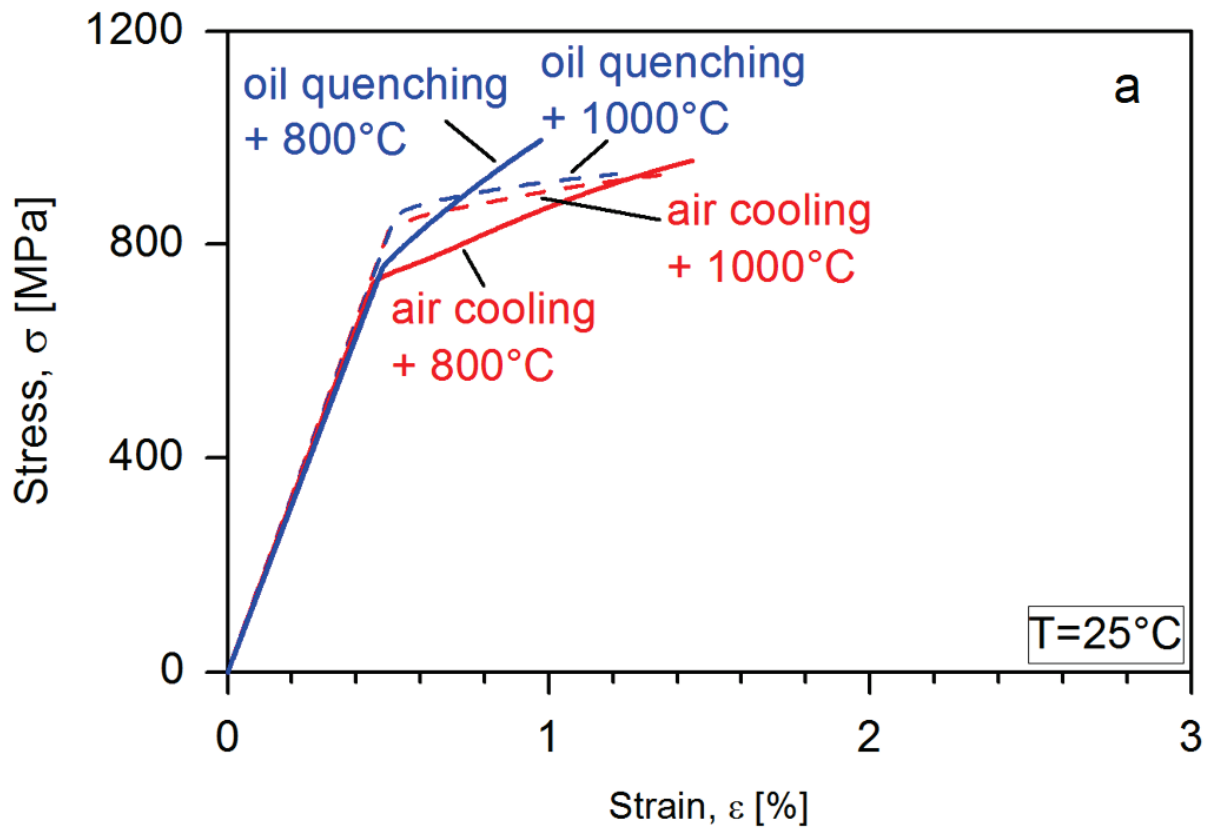


Fig. 9. Tensile test stress-strain curves obtained at room temperature (a) and 700 °C (b) from specimens that were heat treated for 1 h at 1270 °C followed by air cooling and subsequently annealed as indicated.

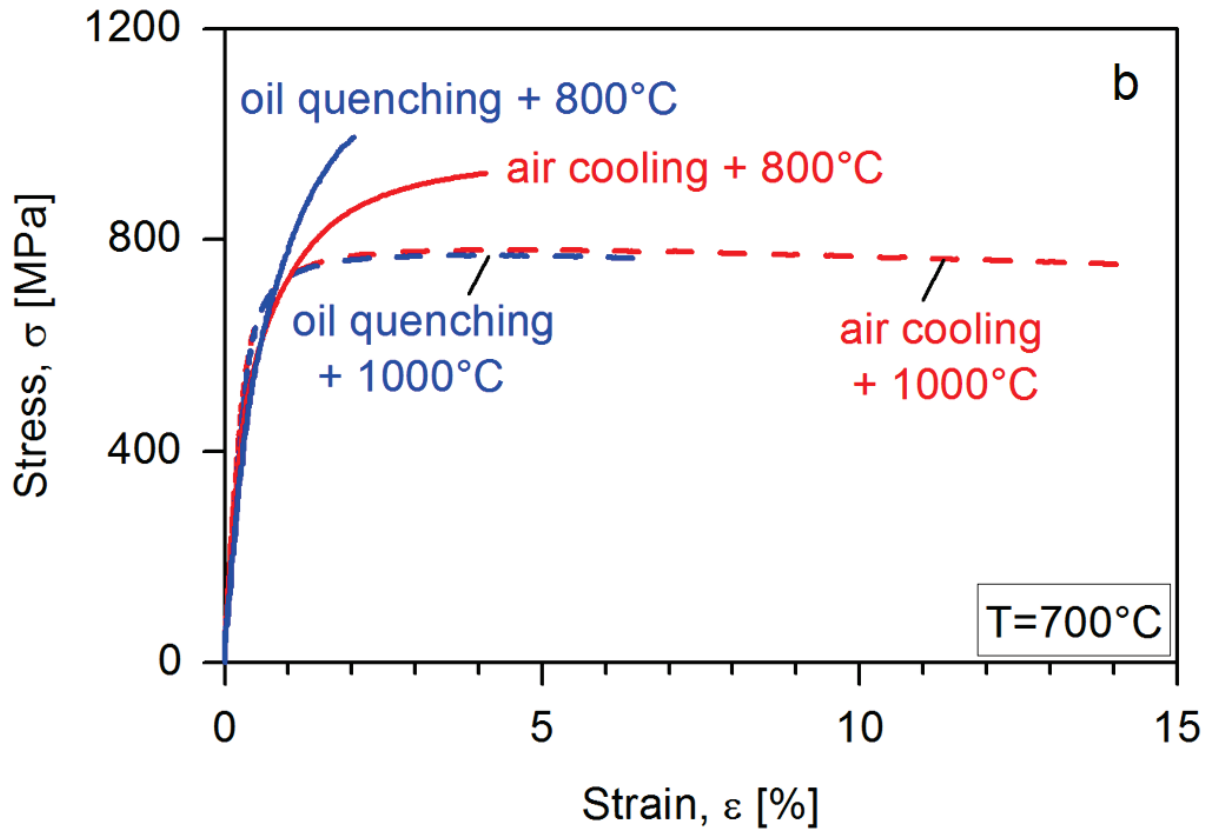


Fig. 9. Tensile test stress-strain curves obtained at room temperature (a) and 700 °C (b) from specimens that were heat treated for 1 h at 1270 °C followed by air cooling and subsequently annealed as indicated.

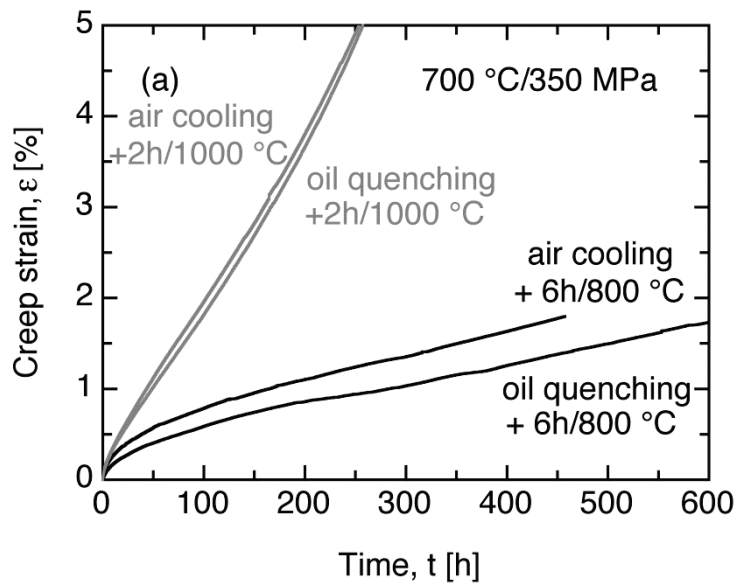


Fig. 10. Creep curves obtained by testing at 700 °C and an initial load of 350 MPa (a) or 250 MPa (b). The specimens were heat treated for 1 h at 1270 °C followed by air cooling and subsequently annealed as indicated.

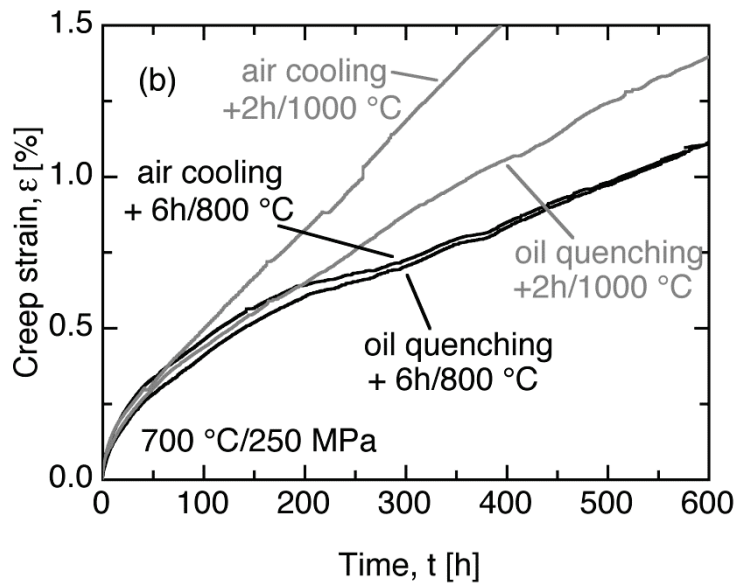


Fig. 10. Creep curves obtained by testing at 700 °C and an initial load of 350 MPa (a) or 250 MPa (b). The specimens were heat treated for 1 h at 1270 °C followed by air cooling and subsequently annealed as indicated.

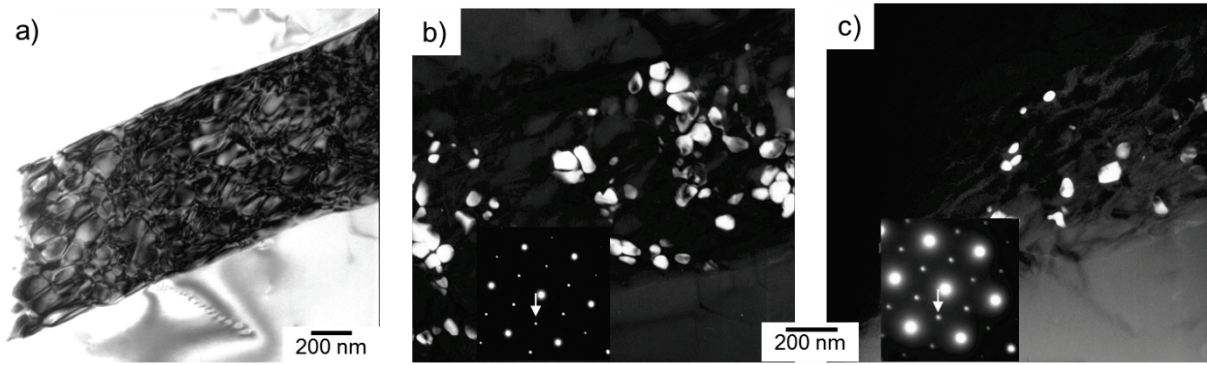


Fig. 11. (a) Bright field TEM micrograph of a β_0/ω_0 grain; (b) the same particle pictured in dark field imaging using the reflection marked in the insert; (c) same particle pictured after tilting the specimen by about 60° using the reflection marked in the insert. The specimen had been heat treated for 1 h at 1270°C followed by furnace-cooling, annealed for 6 h at 800°C and then creep tested at 700°C under an initial load of 250 MPa up to a strain of 3.0 %.

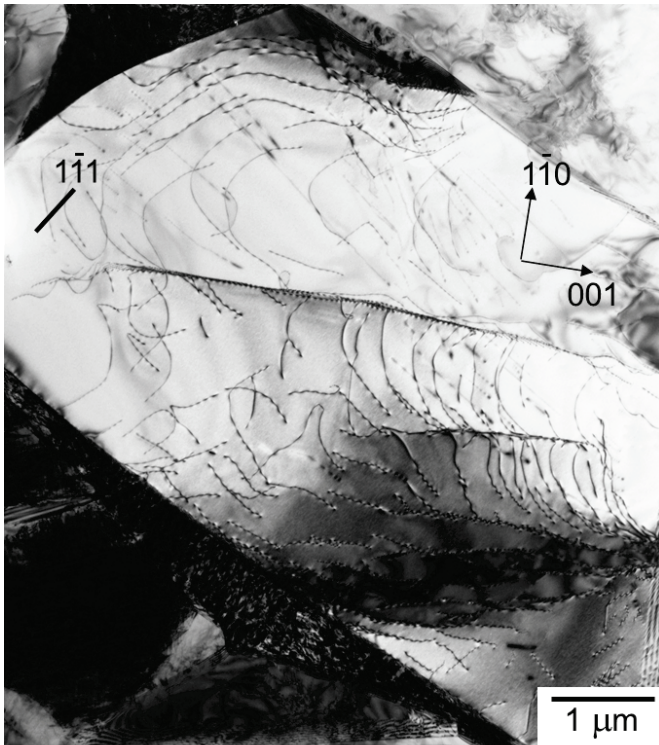


Fig. 12. Dislocation structure in a γ grain imaged by TEM using a $1\bar{1}1$ two beam condition; the grain is oriented near the 110 orientation. The specimen was heat treated for 1 h at 1270 °C followed by furnace-cooling, annealed for 6 h at 800 °C and then creep tested at 700 °C under an initial load of 250 MPa up to a strain of 3.0 %.

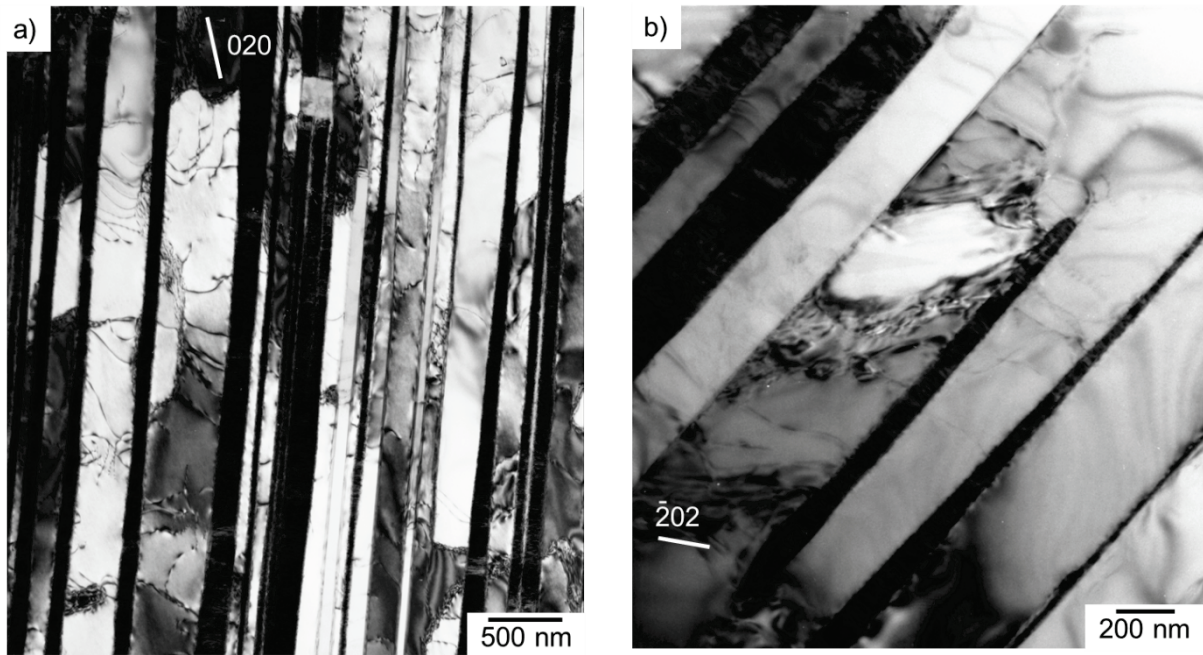


Fig. 13. TEM micrographs of lamellar colonies in the furnace-cooled and creep-deformed specimen; (a) showing dislocations in a number of γ lamellae; (b) showing remnants of dissolving α_2 lamellae. The specimen was heat treated for 1 h at 1270 °C followed by furnace-cooling and 6 h annealing at 800 °C and then creep deformed at 700 °C using an initial load of 250 MPa up to a strain of 3.0 %.

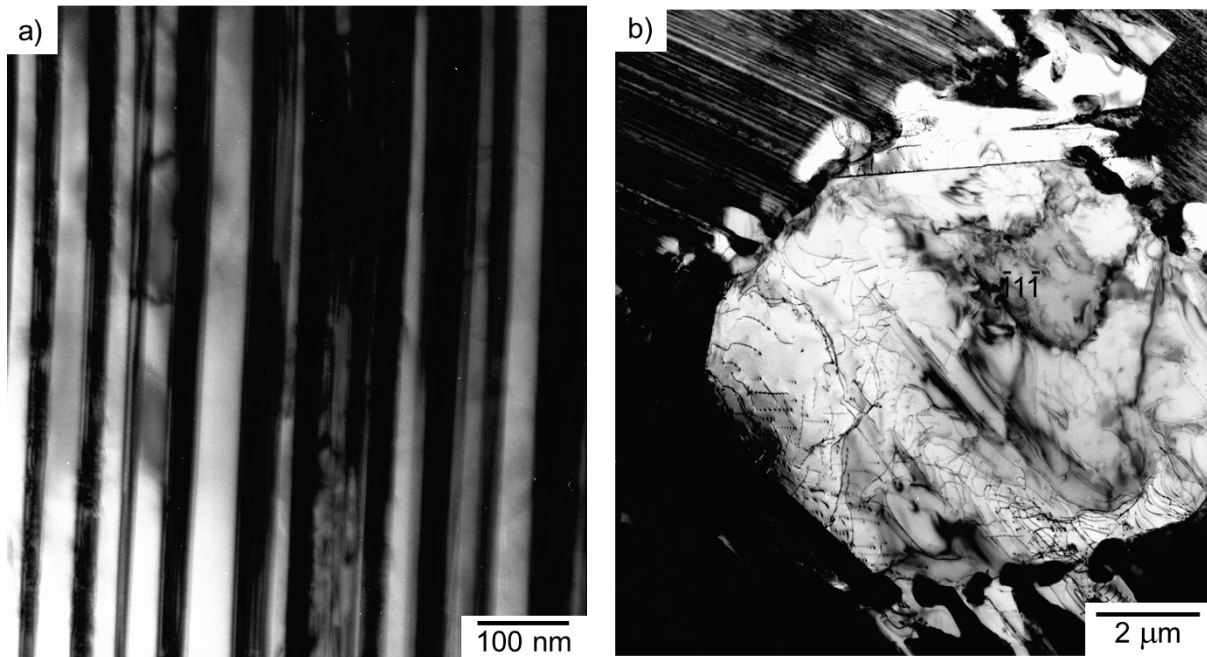


Fig. 14. Microstructure of the air-cooled and creep-deformed specimen; (a) lamellar colony; (b) γ -grain with dislocations oriented along the 110 zone axis pictured using a $\bar{1}1\bar{1}$ two beam condition. The specimen was heat treated for 1 h at 1270 °C followed by air-cooling and 6 h annealing at 800 °C and then creep deformed at 700 °C using an initial load of 250 MPa up to a strain of 2.8 %.